Batholith recorded mesozoic multistage tectonic evolution of the South china block: A case study of the guandimiao intrusions

Jin-Hua Qin, Fan Huang* and Deng-Hong Wang

MNR Key Laboratory of Metallogeny and Mineral Assessment, Institute of Mineral Resources, CAGS, Beijing, China

South China is a well-known grand felsic igneous rocks province. However, it is still controversial and not well understood whether the Mesozoic tectono-magmatic pattern is dominated by the subduction of the paleo-Pacific oceanic plate. In this study, we address this question by concentrating on the long-term evolutionary Guandimiao batholith, which has complex lithofacies with different formation ages and can be a superb record of the Mesozoic tectonic evolution in South China. Geochronologically, four stages of magmatism can be identified combined with previous reports: granodiorite (G1, 239 Ma), biotite monzogranite (G2-1) and two-mica monzogranite (G2-2) (230−203 Ma), granite porphyry (G3, 211−190 Ma), and lamprophyre (L4, 121 Ma). G1 and G2-1 have an affinity with I-type granite and were derived from metabasaltic to metatonalitic sources, whereas G2 and G3 show S-type granite characteristics and were derived from the para-metamorphic basement of the Cathaysia block. The L4 was derived from partial melting of garnet and spinel lherzolite and underwent mixing between Mesoproterozoic pelagic and/or terrigenous sediments and the subcontinental lithosphere mantle (SCLM) of South China. The granitoids of the Guandimiao batholith underwent intensely fractional crystallization of feldspar, Ti-bearing minerals, allanite and monazite. The zircon U−Pb dating of L4 in the Guandimiao batholith completely records the six stages of pre-Mesozoic tectonic events in the SCB. During the Mesozoic, the main body of the Guandimiao batholith (G1, G2-1 and G2-2) recorded the closure of the paleo-Tethys Ocean in the Triassic and the subsequent regional extension of the postcollision. G-3 and L4 of the Guandimiao batholith documented the transition of tectonic and dynamic regimes in the early Yanshanian and the rollback and steep subduction of the paleo-Pacific Ocean in the late Yanshanian.

1 Introduction

South China is a felsic large igneous rock province that developed large intrusions and volcanics with a total outcrop area of nearly 218,090 km². In particular, the outcrop area of granitoids occupies more than 90% of the total area of igneous rock (Zhou et al., 2006). Multiple stages of magmatic activity have been determined using accurate geochronological data (Zhou et al., 2006; Wang et al., 2010; Mao et al., 2011; Mao et al., 2014). Zhou et al. (2006) proposed four main stages of granitic magmatism: 251–234, 234–205, 180–142, and 142–67 Ma. Moreover, the mafic rocks contain three main clusters: the 190–160 Ma group (Zhao et al., 1998; Meng et al., 2012), the 160–110 Ma group (Wang et al., 2003; Wang et al., 2008; Ma et al., 2013) and the 110–80 Ma group (Chen et al., 2008a; Meng et al., 2012; Qin et al., 2020). Numerous models have been proposed for the systematic understanding of the evolutionary history of the regional geology. However, to date, the tectonic regime is not consistently well understood. Li and Li (2007) and Jiang et al. (2015) interpreted extensive igneous rocks in the early Mesozoic as a continual constraint of the plate subduction model of the Paleo-Pacific oceanic plate of the SCB. Wang et al. (2003), Mao et al. (2014), and Li et al. (2014) confirmed that the SCB suffered from the convergence of multiple plates in Indosinia. Subsequently, the postcollisional and postorogenic regimes occurred 234–203 Ma and 190–170 Ma, respectively (Zhou et al., 2006; Mao et al., 2014; Shu et al., 2019). Two supportable mechanisms have been presented with the controversy of whether the subduction of the Pacific Ocean dominated the tectono-magmatic pattern of the SCB in the middle to late Mesozoic (Li, 1990; Gilder et al., 1996; Chen et al., 2014; Li et al., 2014; Qin et al., 2020; Yang et al., 2020).

Batholith generally has complex lithofacies assemblage and long time span. It recorded the imprint of multiple stages of magmatism and thus can be considered an extremely advantageous object for studying the history of regional tectono-magmatic evolution (Hervé et al., 2007; Whalen et al., 2010; Zhao et al., 2012; Deng et al., 2017). Typical batholiths, such as South Patagonian batholiths, recorded magmatic activity over 100 Ma, which is essential for understanding the development of subduction from 157 to 40 Ma (Hervé et al., 2007). The Cumberland batholith (CB) in Canada provides evidence for Paleoproterozoic crustal and orogenic processes of the Trans-Hudson Orogen (Whalen et al., 2010), and the Lincang batholith in West China reveals the suture process of the Changning-Menglian belt (Deng et al., 2017). Thus, further research on Mesozoic batholiths of South China might be the key point for addressing the controversial geodynamic issues in the Mesozoic (Barbarin, 2005; Zhao et al., 2012).

The Guandimiao batholith is located in the middle Qing-Hang paleostylolitic zone in the SCB. Conspicuously, it is a sizeable Mesozoic batholith with a total area of approximately 300 km² that, with formation ages throughout the Mesozoic, could be considered a complete record of Mesozoic tectonic and magmatic events (Wang et al., 2003; Dai et al., 2008; Zhao et al., 2017). Spatially, mafic rocks (MME, lamprophyre) and felsic rocks (granitoids) are concomitant in the Guandimiao batholith. Geochemically, the Guandimiao batholith contains two distinct granitic end-members, I-type granite from the Jingtou area and S-type granite from the Shizhuqiao area (Zhao et al., 2017). Thus, it could also effectively reveal deep crust–mantle interactions and generally trace complicated regional tectonic evolution. Wang et al. (2003), Bai et al. (2014), and Zhao et al. (2017) proposed that the Guandimiao batholith was formed at the 239–220 Ma, which is associated with the post-orogeny regime. Miao (2014) obtained the zircon U-Pb age of 203 ± 1.4 Ma from bitotite granite in Zhoujialing area, which is nearly 20 Ma younger than the previous studies. Dai et al. (2008) reported the occurance of the granite porphyry and lamprophyre and claimed that the dikes are formed at 153 Ma. However, due to lack of systematic geochronological and geochemical investigations, the petrogenesis, geological framework and geodynamic backgrounds for various types of magmatic rocks in the Guandimiao batholith still remain quite unclear.

To confirm the exact chronological sequence, geochemical characteristics, and further discussion of the relationship between intrusions and multiple stages of tectonic setting, we report new LA-ICP–MS zircon U-Pb data and geochemical and Sr-Nd-Pb isotope data for the Guandimiao batholith.

2 Regional geology

The Guandimiao batholith is situated in the northern part of the middle SCB. The SCB consists of the Yangtze Block (YZB) to the west and the Cathaysia Block (CAB) to the east (Figure 1A). The area experienced closure of the YZB and subsequently, the South China folded orogenic multistage intraplate cleavage occurred in the late Neoproterozoic (Li et al., 1999; Li et al., 2001; Li et al., 2002; Greentree et al., 2006; Meng et al., 2012). The Jiuling batholith recorded magmatism in the Neoproterozoic with ages ranging from 848 to 794 Ma (Li et al., 2003; Zhong et al., 2005). During the Phanerozoic, the SCB was in a stable intraplate tectonic environment in South China, dominated by early Paleozoic tectonic stress and early Mesozoic closure of the ancient Tethys Ocean in East Asia (Liu, 1994; Rowley, 1997; Wang et al., 2005a; Mao et al., 2005; Shu, 2012). Subsequently, in the late Mesozoic, the tectonic environment was characterized by multiple periods of compressional and extensional orogeny and the development of widespread depression red basins and depression belts (Xia, 1991; Cheng, 1994; Gilder et al., 1995; Gilder and Courtillot, 1997; Wang et al., 2005b; Yang et al., 2019; Yang et al., 2020). Correspondingly, the famous Zhuguangshan batholith formed 500–90 Ma with a large, exposed area of more than 1,000 km² (Li, 1990; Deng et al., 2012; Zhang et al., 2020).
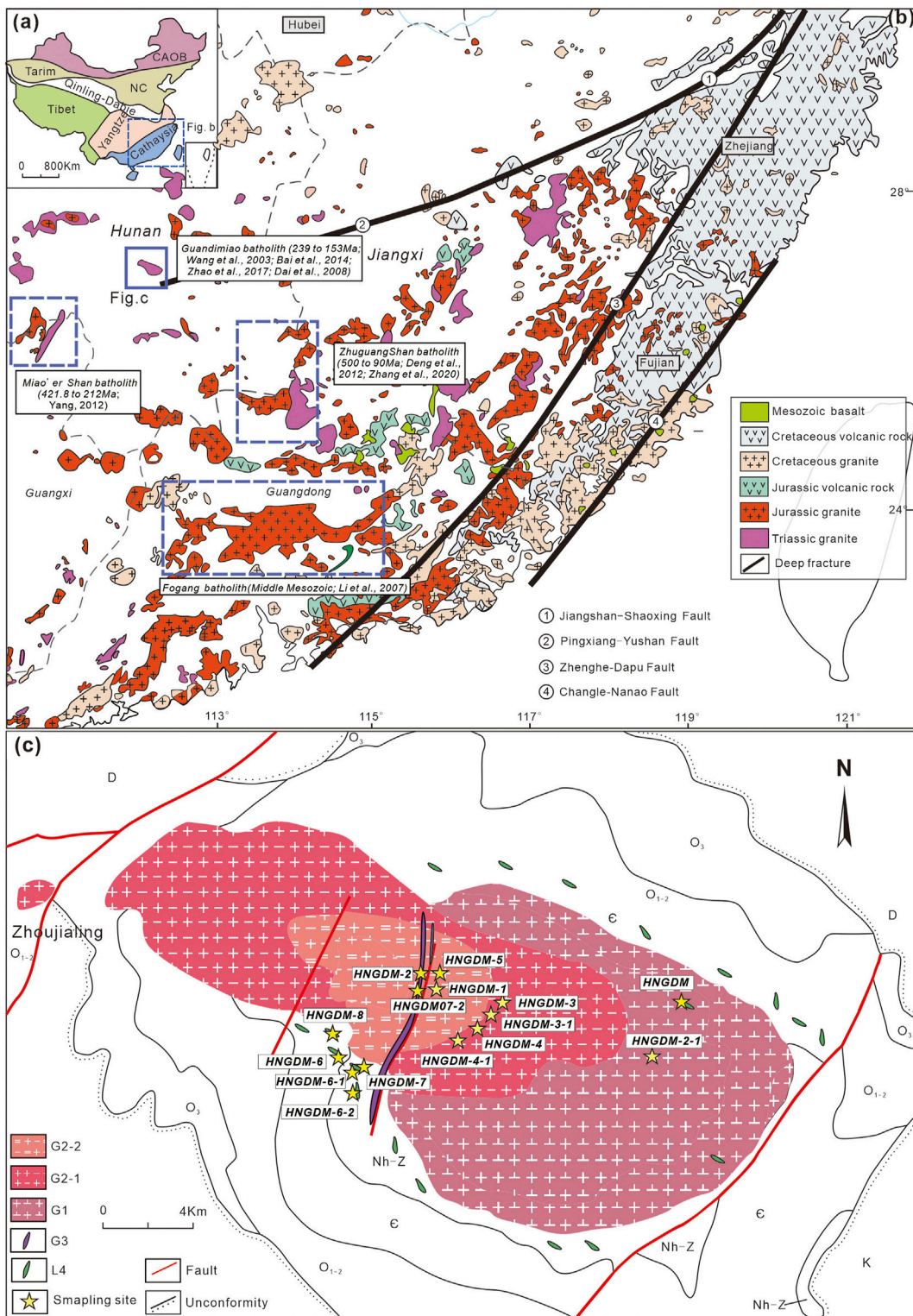
FIGURE 1
(A), Tectonic map of China (after Shu and Zhou, 2002); **(B)**, Regional tectonic map of south China (after Sun, 2006; Wang et al., 2013); **(C)**, Geological map of Guandimiao batholith (after Bai et al., 2014).

Miao'shan-Yuechengling batholith is exposed in the western part of the SCB with emplacement ages from 421.8 to 212 Ma (Yang, 2012). The Fogang batholith had a large volume with a single temporal distribution in the middle Mesozoic (Li et al., 2007). The Guandimiao batholith developed from 239 to 153 Ma (Wang et al., 2003; Dai et al., 2008; Bai et al., 2014; Zhao et al., 2017) (Figure 1B).

Multiple tectonic events and magmatic processes led to the unique geological features around the Guandimiao batholith. Numerous large abyssal faults, including basement faults and surface-cutting faults, are oriented in NE, NW, and E-W directions. "Checkerboard structure pattern" and "circular structures" are typical structural patterns (Zhang, 1984; Liang and Guo, 2002). NE- to NNE-directed subfaults and fractures closely connect with the abyssal faults and serve as necessary conduits for deep fluids. Precambrian to Cenozoic strata crop out. The Guandimiao batholith is located in a typical uplifted dome. In the center of the uplifted region, Precambrian strata are exposed as epi-metamorphic rocks in the Jiangkou Formation (Z_aj) and carbonate in the Dengying Formation (Zd). The Phanerozoic strata are Permian to Ordovician in age and include sandstone of the Tiaomajian Formation (D_2t), limestone and marble of the Qiziqiao Formation (D_2q) and Xikuangshan Formation (D_3x), and limestone of the Hutian Formation ($C_{2+3}h$). The exposed rock assemblages range from acidic to basic and are dominated by five lithofacies: granodiorite (*G1*), biotite monzogranite (*G2-1*), two-mica monzogranite (*G2-2*), dikes [granite porphyry (*G3*) and lamprophyre (*L4*)] (Figure 1C).

3 Petrography

Granodiorite (G1) is the marginal facies and is distributed along the eastern edge of the Guandimiao batholith. It has a medium-coarse granular texture with a mineral assemblage of quartz (~30%) + plagioclase (andesine, An≈40, 40%) + K-feldspar (~20%) + amphibole (~5%) + biotite (~5%) and minor apatite, zircon and magnetite/ilmenite (Figure 2K). Biotite monzogranite (G2-1) was exposed in the center of the Guandimiao batholith and intruded into Lower Ordovician and Upper Cambrian strata (Figure 2B). The mineral assemblage is dominantly plagioclase (~40%), perthitic K-feldspar (~30%), quartz (~20%), and biotite (~10%) with accessory zircon, garnet, magnetite or ilmenite (Figures 2G,I). MMEs, generally 2 × 3 cm in size, are exposed in the interior of the biotite monzogranite in Shuanghekou village (Figure 1C). Two-mica monzogranite (G2-2) occurs locally in Maohedian town (approximately 3 km in length, 1.5 km in width), which is the central facies of the batholith. The central lithological facies is structurally massive with the occurrence of muscovite grains. The mineral assemblage of two-mica granites consists of perthitic K-feldspar (~30%), plagioclase (~35%), quartz (~20%), biotite

(~5%), muscovite (~5%) and magnetite/ilmenite (~2%) with accessory zircon and monazite (Figure 2J). Granite porphyry (G3) occurs in the interior and surroundings of the Guandimiao batholith. The granite porphyry vein is oriented NNE with a width of 5–10 m and intruded into biotite monzogranite (Figures 2A,H). Granite porphyry presents a typical porphyritic structure, and the phenocryst minerals are quartz (20%), K-feldspar (~15%), plagioclase (~10%), and biotite (<5%). Lamprophyre (L4) is exposed in the interior and around the granitic batholith and is 0.5–2 m in width and vertical in occurrence (Figures 2E,F). They are gray–green in color and intruded into Paleozoic silty slate and granitic batholith. Lamprophyre presents lamprophyric texture. The phenocrysts are mainly biotite and plagioclase, occupying 50% vol. Of the whole rocks. Biotite occurs as brown-light brown sheets 0.2–0.4 mm in size (30% vol). Plagioclase occurs as subhedral crystals that are 0.1–0.2 mm in size (approximately 30% vol). The matrix is mafic with extensive epidotization, chloritization, and carbonation (Figure.2L).

4 Sampling and method

15 samples, no obvious weathering or alteration, were collected from the Guandimiao batholith. The granodiorite sample (HNGDM-2-1) and biotite monzogranite samples (HNGDM-4, HNGDM-4-1, HNGDM-3 and HNGDM-3-1) were collected at Lingguandian town. The two-mica monzogranite samples (HNGDM-1 and HNGDM-5) were collected from the outside of Shiqiaopu lead-zinc ore deposit. The granite porphyry samples (HNGDM-2 and HNGDM07-2) were from Shuangjiangkou village. The lamprophyre samples (HNGDM, HNGDM-6, HNGDM-6-1, HNGDM-6-2, HNGDM-7, and HNGDM-8) were collected from the north of Qidong county. 8 out of 15 samples were chosen for accurately geochronological dating, 12 samples were chosen for geochemical analysis and 8 samples for Sr-Nd-Pb isotopic analysis.

4.1 LA–ICP–MS

Zircon U-Pb dating was performed the Institute of Mineral Resources, CAGS, Beijing, using a Finnigan, Neptune inductively coupled plasma mass spectrometer (MC LA-ICP-MS) with a new wave UP213 laser-ablation system. Helium was used as the carrier gas, and the beam diameter was 30 μm with 10-Hz repetition rate and a laser power of 2.5 J/cm^2. Eight ion counters were used to receive the ^{238}U, ^{235}U, ^{232}Th, ^{208}Pb, ^{207}Pb, ^{206}Pb, ^{204}Pb, and ^{202}Hg signals simultaneously, whereas data for ^{208}Pb, ^{232}Th, ^{235}U, and ^{238}U were collected on a Faraday cup. Zircon GJ-1 was used as standard, and Plešovice zircon was used to optimize the mass spectrometer. U, Th, and Pb concentrations were calibrated
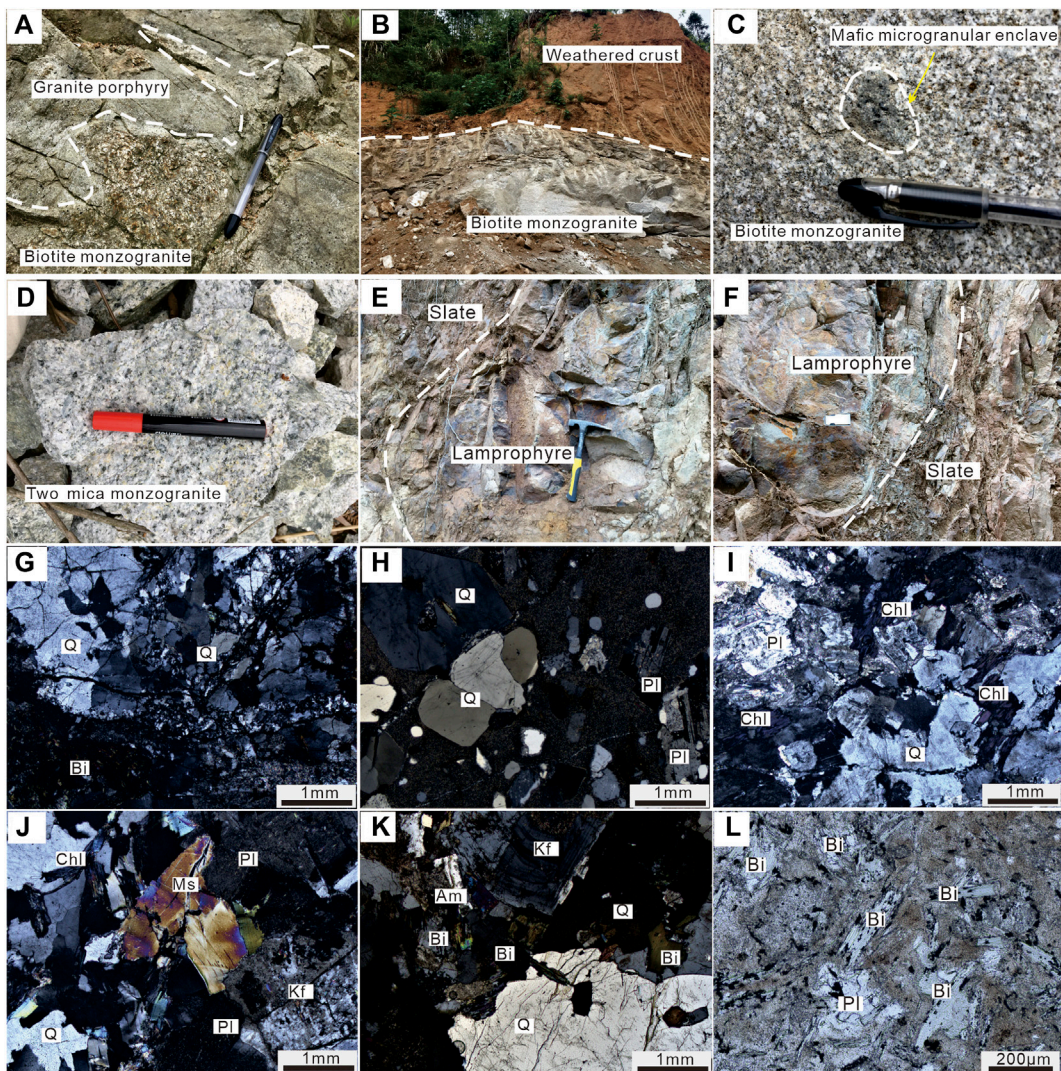
FIGURE 2
Petrographic photograph of Guandimiao batholith; **(A)**, Granite porphyry intruded into biotite monzogranite; **(B)**, Biotite monzogranite profile; **(C)**, MME (mafic microgranular enclave) in biotite monzogranite; **(D)**, Weathered two-mica monzogranite; **(E,F,L)**, Lamprophyre; **(G,I)** Biotite monzogranite; **(H)**, Granite prophyry; **(J)**, Two-mica monzogranite; **(K)**, Granodiorite. Abbreviation: Q-Quarz; Bi-Biotite; Pl-Plagioclase; Chl-Chlorite; Ms-Muscovite; Kf- Potassium feldspar; Am- Amphibole.

using 29 Si as internal standard and zircon M127 U: 923 ppm; Th: 439 ppm; Th/U: 0.475 (Nasdala et al., 2008) as external standard. $^{207}Pb/^{206}Pb$ and $^{206}Pb/^{238}U$ were calculated using the ICP-MS DataCal 4.3 program. Common Pb was not corrected because of the high $^{206}Pb/^{204}Pb$. Abnormally high ^{204}Pb data were deleted. The Plešovice zircon was dated as unknown and yielded a weighted mean $^{206}Pb/^{238}U$ age of 337 ± 2 Ma (2SD, n = 12), which is in good agreement with the recommended $^{206}Pb/^{238}U$ age of 337.13 ± 0.37 Ma (2SD) (Sláma et al., 2008). Age calculations were performed, and concordia diagrams were generated using the Isoplot/Ex 3.0 software (Ludwig, 2003).

4.2 Geochemstry

Whole-rock major, trace and rare earth element concentrations were analyzed at the National Geological Experiment Test Center, Beijing. Whole-rock major elements were analyzed using a plasma spectrometer (PE8300). All results were normalized against the Chinese rock reference standard JY/T015-1996; among them, H_2O^+ is analyzed on the basis of GB/T 14,506.2-2010, FeO contents are normalized to GB/T 14,506.14-2010, LOI contents are normalized to LY/T 1253–1999 and CO_2 contents are normalized to GB 9835–1988. The analytical uncertainties are less than ±2%.

FIGURE 3
Zircon U–Pb concordia diagrams of Guandimiao biotite monzogranite. **(A,C)**, Concordia age diagrams; **(B,D)**, Mean age diagrams.
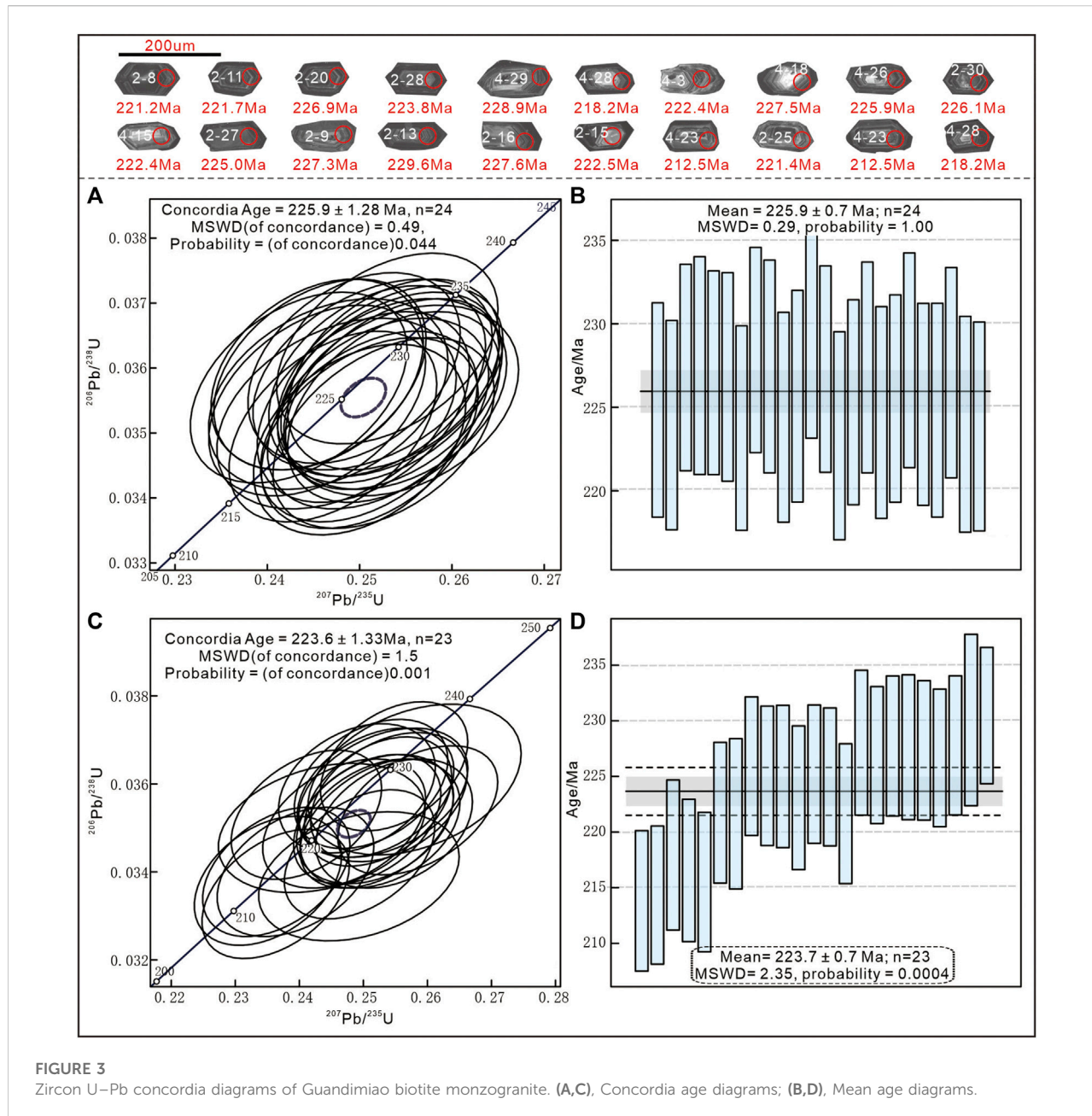
4.3 Sr-Nd-Pb isotope

Fresh samples were ground with an agate mill, and powders were spiked with mixed isotope tracers, dissolved in Teflon capsules with HF + HNO$_3$ acid, and separated by conventional cation exchange techniques. The isotopic measurements were performed on a VG-354 mass spectrometer at the Institute of Geology and Geophysics, Chinese Academy of Sciences. The mass fractionation corrections for Sr and Nd isotope ratios were based on ^{86}Sr/^{88}Sr = 0.1194 and ^{146}Nd/^{144}Nd = 0.7219. Repeat analyses yielded

an ^{87}Sr/^{86}Sr ratio of 0.71023 ± 0.00006 for the NBS-987 Sr standard and a^{143}Nd/^{144}Nd ratio of 0.511845 ± 0.000012 for the La Jolla standard. For Pb isotope determinations, 200 mg of powder was weighed into a Teflon vial, spiked and dissolved in concentrated HF at 80˚C for 72 h. Pb was separated and purified by conventional cation exchange techniques (AG1 × 8,200–400 resin) with diluted HBr as an eluant. Isotopic ratios were measured with a VG-354 mass spectrometer at the Institute of Geology and Geophysics. Repeat analyses of NBS981 yielded ^{204}Pb/^{206}Pb = 0.05897 ± 15, ^{207}Pb/^{206}Pb = 0.91445 ± 80, and ^{208}Pb/^{206}Pb = 2.16170 ± 180. Detailed descriptions of the analytical
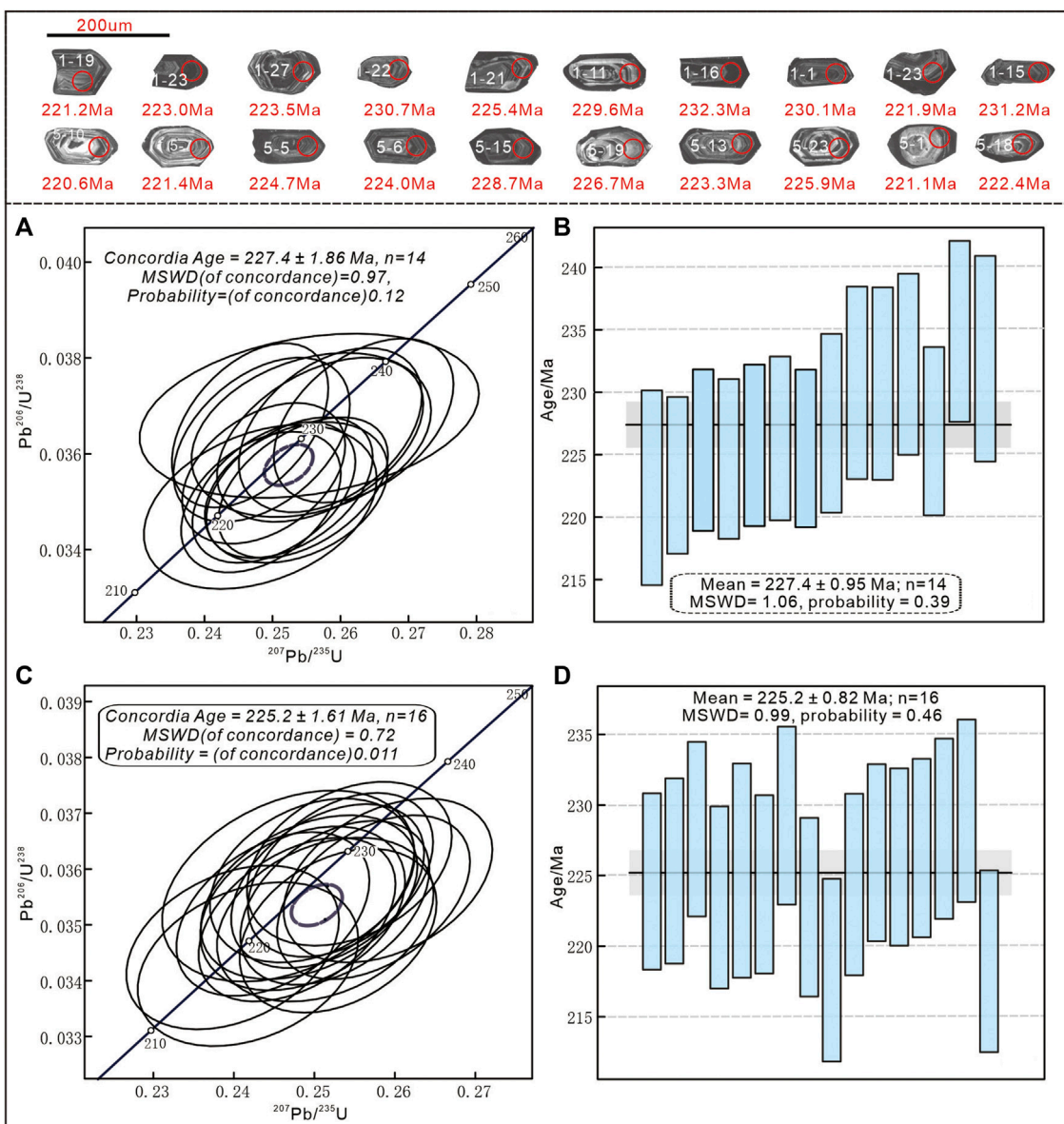
FIGURE 4
Zircon U−Pb concordia diagrams of Guandimiao two-mica monzogranite. **(A,C)**, Concordia age diagrams; **(B,D)**, Mean age diagrams.

techniques are given elsewhere (Zhang et al., 2002, and references therein).

5 Results

5.1 U-Pb chronology

5.1.1 G2-1

Zircons are long and columnar with length-to-width ratios close to 2:1. The sizes of zircons are between 100 and 150 μm. The edges of the zircons were obviously corroded. The U contents range from 446.6 to 1,515.8 ppm. Th contents range from 340.1 to 3,675.8 ppm. Th/U ratios varied from 0.4 to 1.7 (Table 1). The $^{206}Pb/^{238}U$ ages of sample HNGDM-2 are between 212.0 and 229.6 Ma, and yield the concordia age and mean age (n = 24) are 225.9 ± 1.28 Ma (MSWD = 0.49) and 225.9 ± 0.7 Ma (MSWD = 0.29), respectively (Figures 3A,B). The $^{206}Pb/^{238}U$ ages of Sample HNGDM-4 range from 236.1 to 207.6 Ma, and the concordia age and mean age (n = 19) of the zircon grains are 223.6 ± 1.3 Ma (MSWD = 1.5) and 223.7 ± 1.3 Ma (MSWD = 2.35), respectively (Figures 3C,D).

FIGURE 5
Zircon U−Pb concordia diagrams **(A)** and typical CL images **(B)** of Guandimiao granite porphyry; Zircon U−Pb concordia diagrams of Guandimiao lamprophyre **(C,D)**. The black circles in a and b represent $^{206}Pb/^{238}U$ ages of group1 zircons, the blue circles represent $^{206}Pb/^{238}U$ ages of group 2 zircons.
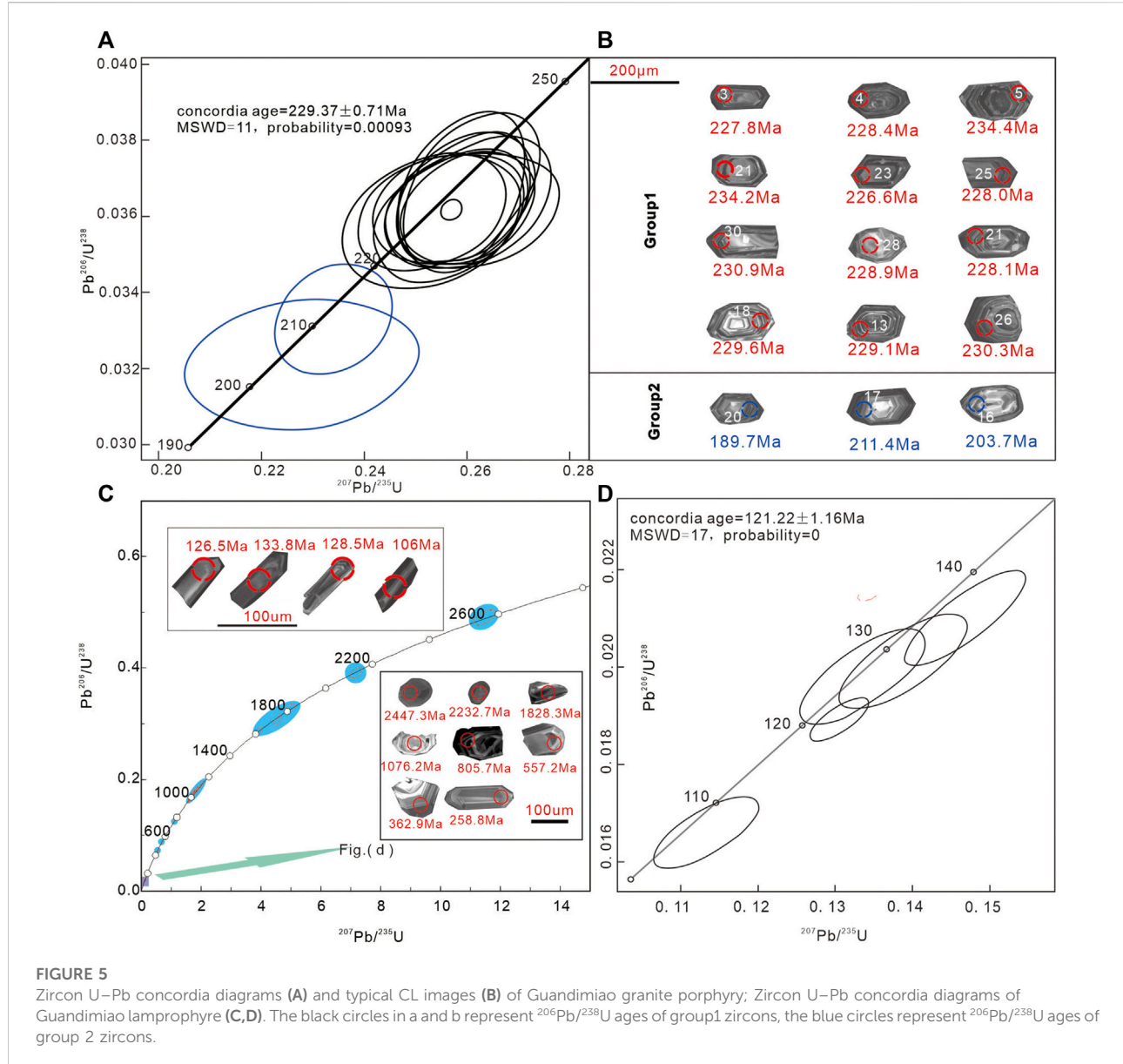
5.1.2 G2-2

Zircons exhibit length-to-width ratios between 1:1 and 2:1 and sizes of 100–200 μm. Most zircon grains developed obvious oscillatory zoning (Figure 4). The U contents range from 53.3 to 4,703.3 ppm (except for one spot value up to 9,301.8 ppm), Th contents range from 54.3 to 4,333.7 ppm (except for one spot value up to 6,293.6.8 ppm), and the Th/U ratios range from 0.5 to 1.9, suggesting an igneous origin (Rubatto, 2002; Wu and Zhen, 2004). Out of 30 spots in sample HNGDM-1, 14 analyses yield $^{206}Pb/^{238}U$ ages of 221.2–233.2 Ma, with a concordia U-Pb age of 227.4 ± 1.86 Ma (MSWD = 0.97) and a mean age of 227.41 ± 0.95 Ma (MSWD = 1.06) (Figures 4A,B). The $^{206}Pb/^{238}U$ ages of Sample HNGDM5-1 range from 217.3 to 228.7 Ma, with a

concordia U-Pb age of 225.19 ± 1.61 Ma (MSWD = 0.72) and a mean age of 225.20 ± 0.82 Ma (MSWD = 0.99, n = 16) (Figures 4C,D).

5.1.3 G3

Zircons developed obvious oscillatory zoning. They exhibit length-to-width ratios from 1:1 to 2:1 with sizes from 100 to 200 μm (Figure 5B). U contents range from 516 to 3,309.6 ppm, Th contents range from 127.1 to 6,116.0 ppm, and Th/U ratios range from 0.1 to 2.2. Thirty spot analyses yield $^{206}Pb/^{238}U$ ages of 189.7–234.4 Ma. Two groups of $^{206}Pb/^{238}U$ ages can be identified. The first group is from 219.5 to 234.4 Ma with a concordia U-Pb age of 229.37 ± 0.71 Ma (MSWD = 2.6) (Figure 5A). The $^{206}Pb/$

FIGURE 6
(A), TAS classification diagram of Guandimiao batholith; (B), SiO$_2$ versus K$_2$O diagram; (C), A/NK versus A/CNK diagram; (D), K$_2$O versus SiO$_2$ diagram.
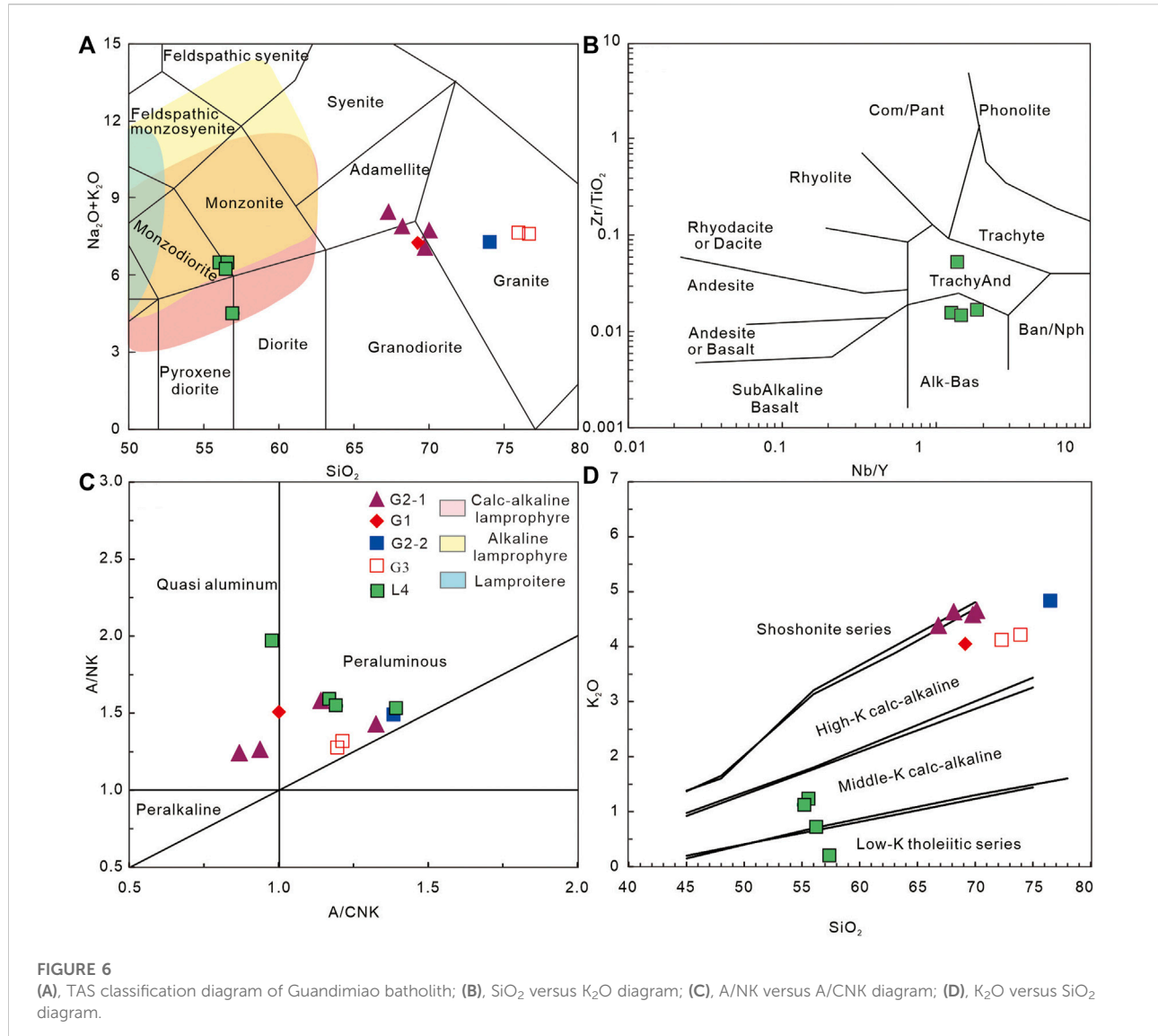
^{238}U ages of the second group range from 189.7 to 211.4 Ma (Figure 5A).

5.1.4 L4

Two distinct groups of zircons were identified. The first group of zircon grains are complex and exhibits length-to-width ratios from 1:1 to 2:1 and sizes from 50 to 200 μm, Most of them developed obvious oscillatory zoning and are generally incomplete in shape, wheras a small amount is smaller in size (50–100 μm) and round in shape. The second group exhibits length-to-width ratios from 3:1 to 4:1 and sizes of approximately 100–150 μm with U contents from 249.8 to 1,195.2 ppm, Th contents from 324.4 to 1,348.3 ppm, and Th/U ratios from 1.0 to 1.3. Out of 61 spot analyses of *L4*, 4 analysis points yield ^{206}Pb/^{238}U

ages of 106.0–133.8 Ma, with a concordia U-Pb age of 121.22 ± 1.16 Ma (MSWD = 7) (Figures 5C,D). The first group of zircons exhibits a long-term span and contains at least nine stages of magmatism 1) 217.7–227.8 Ma; 2) 240.6–268.0 Ma; 3) 295.9–379.6 Ma; 4) 405.3–466.8 Ma; 5) 539.1–615.4 Ma; 6) 769.7–842.8 Ma; 7) 972.4–1,135.0 Ma; 8) 1,625.9–1931.6 Ma, and 9) 2,114.4–2,573.1 Ma, which could reveal the long chronological evolutionary history of South China.

5.2 Geochemistry

The obtained geochemical result of samples from Guandimiao Batholith are listed in Table 2.

FIGURE 7
Rare earth element pattern and spidergrams of Guandimiao batholith (Standardized values according to Sun and McDonough, 1989); **(A,B)**, Standardization diagram of chondrite meteorites of REE; **(C,D)**, normalization diagram of the primitive mantle of trace elements.
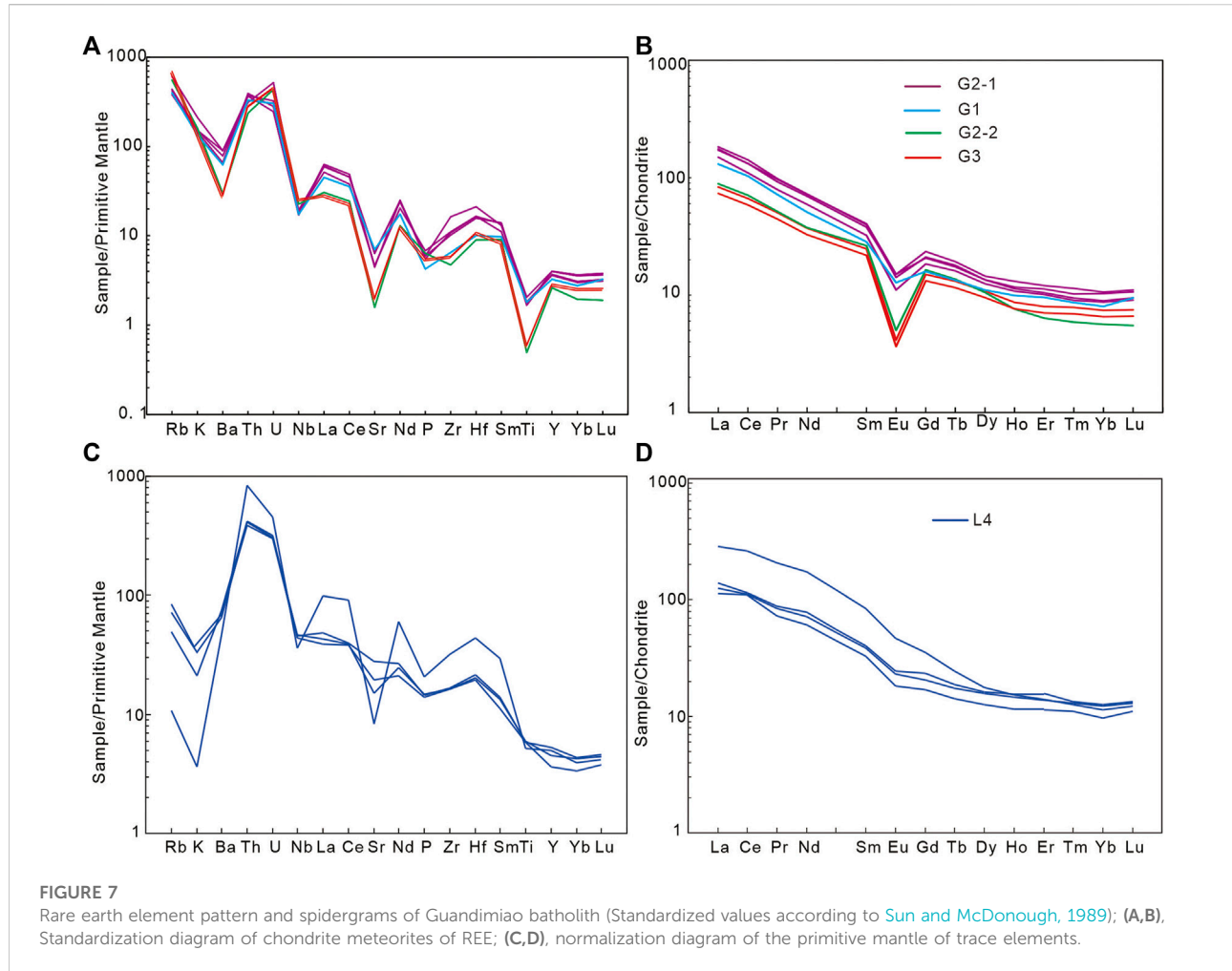
G1 has low SiO_2 (69.29 wt%) and total alkalis (ALK = Na_2O + K_2O) (7.27 wt%) and higher Al_2O_3 (14.6 wt%), MgO (1.58 wt%), and CaO (2.7 wt%). The A/CNK and A/NK values are 1.00 and 1.51, respectively. G2-1 has high Al_2O_3 (14.36–14.71 wt%), ALK (7.76–8.53 wt%) and moderate SiO_2 (67.9–70.1 wt%) and FeO^T (2.96–3.39 wt%) contents and K/Na ratios (0.69–1.82). The ratios of A/CNK are 0.89–1.32, and those of A/NK are 1.24–1.58. The G2-2 have high contents of SiO_2 (74.09–75.2 wt%), ALK (6.43–7.30) and K/Na ratios (1.37–1.67) but low MgO (0.39–0.44 wt%), CaO (0.26–0.41 wt%), and FeO^T (1.22–1.47 wt%) contents.The G-3 is similar to the G2-2 but have higher content of SiO_2 (76.7 wt%), K_2O (4.84 wt%), ALK (7.63 wt%). L4 is characterized by low contents of SiO_2 (55.43–57.14 wt%), K_2O (0.11–1.01 wt%), ALK (4.12–6.70 wt%) and high contents of Al_2O_3 (12.83–17.02 wt%), FeO^T (6.66–7.31 wt%) and MgO (0.86–7.19 wt%). The SiO_2 versus (Na_2O + K_2O) and Zr/TiO_2 versus Nb/Y diagrams suggest monzonite-diorite affinity for G1 and G2-1, granite affinity for G2-2 and G3, and calc-alkaline lamprophyre for L4 (Figures 6A,B). On the

A/CNK versus A/NK diagram and SiO_2 versus K_2O diagram, all samples plot in the metaluminous-peraluminous field, whereas G1, G2-1, G2-2, and G3 hold middle-high K calc-alkaline (CA) characteristics, and L4 has middle to low K calc-tholeiitic series affinity (Figures 6C,D).

The chondrite-normalized REE patterns of G2-2 and G3 show strongly negative Eu anomalies (δEu = 0.21–0.23) and have obviously lower differentiation of LREEs and HREEs [$(La/Yb)_N$ = 10.54–11.29, LREEs/HREEs = 8.84–9.81] than G1 and G2-1. The REE pattern of L4 has negative slopes with no obvious negative Eu anomalies (Eu/Eu* = 0.73–0.78). Except for HNGDM-7, L4 shows the lowest fractionation of REEs (($La/Yb)_N$ = 9.66–10.98, LREEs/HREEs = 9.80–11.35). Spider diagrams normalized by a primitive mantle show entiched Rb, Th, U, La, Ce, Nd, Zr, and Hf and depleted Ba, Nb, Ce, P, and Ti for G1 and G2-1 (Figure 7A). G2-2 and G-3 are enriched in Rb, K, Th, U, La, Ce, Hf, and Y and depleted in Ba, Nb, Sr, Zr, and Ti (Figure 7B). L4 is enriched in Rb, Th, U, Nd, and Hf but depleted in K, Nb, Sr, and P. Sample HNGDM-7 of L4 obviously deviates from the main trend and presents stronger K, Nb, and Sr

TABLE 1 LA–ICP–MS U–Pb analysis results of the Guandimiao batholith.

Spot	WB/10⁻⁶			Isotope ratio (± 1σ)						Isotope age (Ma) (± 1σ)					
	Th	U	Th/U	$^{207}Pb/^{206}Pb$		$^{207}Pb/^{235}U$		$^{206}Pb/^{238}U$		$^{207}Pb/^{206}Pb$		$^{207}Pb/^{235}U$		$^{206}Pb/^{238}U$	
				Ratio	Erro	Ratio	Erro	Ratio	Erro	Age	Erro	Age	Erro	Age	Erro
								G2-2							
HNGDM-1-18	1907.2	2079.4	0.9	0.0516	0.0012	0.2484	0.0055	0.0336	0.0006	267.9	50.2	225.3	4.5	213.2	3.8
HNGDM-1-28	1,552.9	1,219.3	1.3	0.0514	0.0012	0.246	0.006	0.0337	0.0006	257.2	54.5	223.3	4.9	213.3	3.8
HNGDM-1-26	957.1	3,665.1	0.3	0.0636	0.0013	0.3169	0.0064	0.0344	0.0006	728.9	42.7	279.5	4.9	218.2	3.8
HNGDM-1-19	1,341.1	1,186.1	1.1	0.0491	0.0014	0.2482	0.007	0.0349	0.0007	152.7	63.4	225.1	5.7	221.2	4.0
HNGDM-1-23	905.6	992.9	0.9	0.0501	0.001	0.2483	0.0048	0.035	0.0006	201.4	44.8	225.2	3.9	221.9	3.9
HNGDM-1-3	222.6	472.7	0.5	0.0528	0.0012	0.2535	0.0055	0.0352	0.0006	321.0	48.8	229.4	4.5	223.0	3.9
HNGDM-1-14	648.3	846.5	0.8	0.0511	0.001	0.2502	0.0049	0.0352	0.0006	247.1	45.2	226.8	4.0	223.0	3.9
HNGDM-1-12	1,645	2,378.6	0.7	0.0687	0.0014	0.3649	0.0075	0.0352	0.0006	888.5	42.0	315.9	5.6	223.2	3.9
HNGDM-1-27	287.5	528.5	0.5	0.051	0.001	0.2525	0.005	0.0353	0.0006	241.1	46.1	228.6	4.1	223.5	3.9
HNGDM-1-10	297	636.9	0.5	0.0514	0.001	0.2545	0.0051	0.0353	0.0006	259.0	45.8	230.2	4.1	223.7	3.9
HNGDM-1-20	3,090.9	1913.4	1.6	0.1226	0.0024	0.6158	0.0116	0.0355	0.0006	1993.8	33.9	487.2	7.3	224.9	3.9
HNGDM-1-21	780.8	810.5	1.0	0.0495	0.001	0.2487	0.0049	0.0356	0.0006	171.4	46.1	225.5	4.0	225.4	3.9
HNGDM-1-11	1961.5	1744.1	1.1	0.0528	0.001	0.2768	0.0053	0.0363	0.0006	319.5	43.6	248.1	4.2	229.6	4.0
HNGDM-1-29	754.6	557.7	1.4	0.0504	0.0011	0.2484	0.0053	0.0363	0.0007	211.3	48.9	225.3	4.3	229.6	4.0
HNGDM-1-1	1,170.5	894.1	1.3	0.0471	0.0011	0.257	0.0062	0.0363	0.0007	55.2	56.6	232.2	5.0	230.1	4.1
HNGDM-1-22	1,040.5	762.8	1.4	0.0482	0.0014	0.2557	0.0072	0.0364	0.0007	109.6	65.0	231.2	5.8	230.7	4.1
HNGDM-1-15	1,294.5	1,178.7	1.1	0.0501	0.0011	0.2585	0.0055	0.0365	0.0007	198.8	48.6	233.4	4.4	231.2	4.1
HNGDM-1-5	2,513.1	1,596.6	1.6	0.0581	0.0011	0.3011	0.0056	0.0365	0.0007	533.8	42.0	267.2	4.4	231.3	4.0
HNGDM-1-8	4,404.5	2,353.8	1.9	0.05	0.001	0.2467	0.0047	0.0366	0.0007	196.6	44.6	223.9	3.8	231.5	4.0
HNGDM-1-16	1,072	2,240.7	0.5	0.0525	0.0011	0.2634	0.0054	0.0367	0.0007	307.3	46.3	237.4	4.3	232.3	4.1
HNGDM-1-7	1,006.1	762	1.3	0.0483	0.0019	0.2554	0.0102	0.0368	0.0007	115.3	88.8	230.9	8.2	233.2	4.4
HNGDM-1-13	2,472.4	2,243.4	1.1	0.067	0.0013	0.3565	0.0067	0.0374	0.0007	837.4	39.4	309.6	5.0	236.4	4.1
HNGDM-1-6	1905.4	2,195.6	0.9	0.0518	0.0011	0.2696	0.0054	0.0383	0.0007	274.5	45.6	242.4	4.3	242.3	4.2
HNGDM-1-17	2,197.4	2,829.6	0.8	0.1495	0.0029	0.7968	0.0148	0.0385	0.0007	2,340.7	32.2	595.0	8.4	243.4	4.2
HNGDM-1-25	1,297.4	1,399.1	0.9	0.1493	0.0029	0.8237	0.0158	0.0391	0.0007	2,337.4	32.9	610.1	8.8	247.5	4.3
HNGDM-1-24	860.9	696.3	1.2	0.0501	0.0011	0.2736	0.0062	0.0395	0.0007	200.5	51.5	245.5	4.9	249.5	4.4
HNGDM-1-2	1,001.1	4,703.1	0.2	0.196	0.0037	1.0946	0.02	0.0408	0.0007	2,792.9	30.4	750.7	9.7	257.8	4.5
HNGDM-1-30	6,293.6	1,341.7	4.7	0.3095	0.0059	1.9078	0.0351	0.0425	0.0008	3,518.5	28.9	1,083.8	12.3	268.4	4.7
HNGDM-1-4	988	4,462	0.2	0.1513	0.0029	0.8726	0.0161	0.0427	0.0008	2,361.0	31.9	637.0	8.7	269.2	4.7
HNGDM-1-9	4,333.7	9,301.8	0.5	0.4406	0.0083	2.9242	0.0533	0.0491	0.0009	4,053.6	27.7	1,388.2	13.8	308.7	5.3
HNGDM-5-1_1	779.5	1,270.9	0.6	0.0515	0.0011	0.2530	0.0050	0.0349	0.0006	263.8	46.3	229.0	4.0	221.1	3.8
HNGDM-5-1_2	350.3	338.5	1.0	0.0668	0.0015	0.3612	0.0078	0.0396	0.0007	831.6	44.9	313.1	5.8	250.0	4.4
HNGDM-5-1_3	562.6	819.9	0.7	0.0466	0.0012	0.2555	0.0064	0.0343	0.0006	27.5	57.7	231.0	5.1	217.5	3.8
HNGDM-5-1_4	1,491.3	1,649.7	0.9	0.0562	0.0011	0.2903	0.0055	0.0355	0.0006	458.8	43.6	258.8	4.3	224.9	3.9
HNGDM-5-1_5	339.8	440.7	0.8	0.0496	0.0011	0.2494	0.0055	0.0355	0.0006	178.3	51.2	226.1	4.4	224.7	3.9
HNGDM-5-1_6	1963.6	3,203.5	0.6	0.0597	0.0012	0.3079	0.0058	0.0354	0.0006	592.8	41.4	272.6	4.5	224.0	3.9
HNGDM-5-1_7	910.9	1,453.6	0.6	0.0525	0.0011	0.2570	0.0049	0.0349	0.0006	305.6	44.9	232.2	4.0	221.4	3.8
HNGDM-5-1_8	821.5	1,158.8	0.7	0.0515	0.0010	0.2533	0.0047	0.0359	0.0006	260.9	43.9	229.2	3.8	227.6	3.9
HNGDM-5-1_9	1,322.1	1,478.9	0.9	0.0609	0.0012	0.3011	0.0058	0.0368	0.0007	634.6	42.4	267.2	4.5	232.9	4.0
HNGDM-5-1_10	603.6	983.2	0.6	0.0501	0.0011	0.2582	0.0056	0.0348	0.0006	199.6	50.5	233.2	4.5	220.6	3.9
HNGDM-5-1_11	54.3	53.3	1.0	0.0499	0.0010	0.2479	0.0050	0.0351	0.0006	189.9	47.9	224.9	4.1	222.5	3.9
HNGDM-5-1_12	284.2	331.1	0.9	0.0493	0.0013	0.2468	0.0064	0.0357	0.0007	161.1	59.2	224.0	5.2	226.1	4.1
HNGDM-5-1_13	510.0	646.3	0.8	0.0495	0.0011	0.2486	0.0052	0.0353	0.0006	170.0	49.8	225.4	4.3	223.3	3.9
HNGDM-5-1_14	537.8	671.1	0.8	0.0524	0.0014	0.2324	0.0060	0.0335	0.0006	303.4	57.9	212.1	4.9	212.3	3.8
HNGDM-5-1_15	337.8	473.6	0.7	0.0508	0.0011	0.2544	0.0052	0.0361	0.0006	233.8	47.6	230.1	4.2	228.7	4.0
HNGDM-5-1_16	969.0	1,158.8	0.8	0.0491	0.0010	0.2449	0.0049	0.0352	0.0006	154.5	47.4	222.5	4.0	223.3	3.9
HNGDM-5-1_17	133.7	192.2	0.7	0.0493	0.0012	0.2418	0.0056	0.0343	0.0006	161.6	54.5	219.9	4.6	217.3	3.8

TABLE 1 (*Continued*) LA–ICP–MS U–Pb analysis results of the Guandimiao batholith.

Spot	WB/10⁻⁶			Isotope ratio (± 1σ)						Isotope age (Ma) (± 1σ)					
	Th	U	Th/U	$^{207}Pb/^{206}Pb$		$^{207}Pb/^{235}U$		$^{206}Pb/^{238}U$		$^{207}Pb/^{206}Pb$		$^{207}Pb/^{235}U$		$^{206}Pb/^{238}U$	
				Ratio	Erro	Ratio	Erro	Ratio	Erro	Age	Erro	Age	Erro	Age	Erro
HNGDM-5-1_18	436.8	601.3	0.7	0.0519	0.0012	0.2514	0.0055	0.0351	0.0006	279.5	50.3	227.7	4.5	222.4	3.9
HNGDM-5-1_19	386.7	479.6	0.8	0.0494	0.0011	0.2498	0.0052	0.0358	0.0006	168.7	48.9	226.4	4.2	226.7	3.9
HNGDM-5-1_20	1,446.4	2051.6	0.7	0.0510	0.0010	0.2526	0.0048	0.0354	0.0006	241.9	45.1	228.6	3.9	224.0	3.9
HNGDM-5-1_21	575.9	843.2	0.7	0.0502	0.0010	0.2517	0.0049	0.0357	0.0006	203.9	46.6	228.0	4.0	226.0	3.9
HNGDM-5-1_22	636.0	860.3	0.7	0.0519	0.0010	0.2574	0.0049	0.0355	0.0006	280.4	45.0	232.6	4.0	224.7	3.9
HNGDM-5-1_23	934.8	1,201.2	0.8	0.0528	0.0011	0.2643	0.0053	0.0357	0.0006	319.8	46.6	238.1	4.3	225.9	3.9
HNGDM-5-1_24	2,139.8	2,761.3	0.8	0.0523	0.0011	0.2592	0.0053	0.0358	0.0006	298.3	47.2	234.0	4.3	226.6	3.9
HNGDM-5-1_25	386.2	595.3	0.6	0.0470	0.0011	0.2399	0.0054	0.0346	0.0006	48.6	53.8	218.4	4.4	219.5	3.8
G2-1															
HNGDM-4-24	343.7	419.1	0.8	0.0552	0.0015	0.2505	0.0068	0.0327	0.0006	420.6	58.7	227.0	5.5	207.6	3.8
HNGDM-4-23	859.3	976.9	0.9	0.0494	0.001	0.2363	0.0047	0.0335	0.0006	167.6	47.2	215.4	3.8	212.5	3.7
HNGDM-4-20	1,069.9	2071.1	0.5	0.0525	0.0011	0.2351	0.0047	0.0338	0.0006	308.3	46.3	214.4	3.9	214.0	3.7
HNGDM-4-25	274.5	426.6	0.6	0.053	0.0014	0.2493	0.0064	0.0339	0.0006	329.1	57.6	226.0	5.2	214.8	3.9
HNGDM-4-19	445.3	425.5	1.0	0.0515	0.0011	0.2394	0.005	0.034	0.0006	262.8	48.6	217.9	4.1	215.5	3.8
HNGDM-4-13	658.4	1,271.7	0.5	0.0491	0.001	0.2364	0.0047	0.034	0.0006	154.1	47.4	215.5	3.8	215.6	3.7
HNGDM-4-11	1,465	1,466.9	1.0	0.054	0.0011	0.258	0.0048	0.0343	0.0006	369.8	43.7	233.1	3.9	217.6	3.7
HNGDM-4-28	1,041.9	1,023.3	1.0	0.0505	0.001	0.2494	0.0048	0.0344	0.0006	219.5	46.1	226.1	3.9	218.2	3.8
HNGDM-4-9	1,236.3	1737.5	0.7	0.0472	0.0013	0.2435	0.0066	0.035	0.0006	57.2	63.6	221.3	5.4	221.8	3.9
HNGDM-4-3	1,019.8	940.8	1.1	0.0517	0.0011	0.2548	0.005	0.0351	0.0006	270.1	45.7	230.5	4.0	222.4	3.8
HNGDM-4-15	660	763.8	0.9	0.0505	0.0011	0.2526	0.0051	0.0351	0.0006	216.2	47.8	228.6	4.2	222.4	3.9
HNGDM-4-4	1,140.6	1,320	0.9	0.0532	0.0011	0.267	0.0055	0.0351	0.0006	336.1	47.3	240.3	4.4	222.5	3.9
HNGDM-4-7	1,157.7	1,358.3	0.9	0.051	0.001	0.2521	0.0049	0.0351	0.0006	241.3	46.1	228.3	4.0	222.5	3.8
HNGDM-4-1	473.8	648.3	0.7	0.0515	0.0011	0.247	0.0052	0.0351	0.0006	260.9	48.9	224.1	4.2	222.6	3.9
HNGDM-4-14	561.3	868.7	0.6	0.0512	0.0011	0.2518	0.005	0.0352	0.0006	250.0	46.6	228.0	4.0	222.9	3.9
HNGDM-4-12	660.2	1,247.2	0.5	0.0508	0.001	0.2506	0.0047	0.0352	0.0006	233.7	44.8	227.0	3.8	223.2	3.8
HNGDM-4-22	386.3	558.4	0.7	0.0495	0.001	0.2411	0.0048	0.0353	0.0006	171.5	47.3	219.3	3.9	223.6	3.9
HNGDM-4-2	1,090.5	1,271	0.9	0.0509	0.001	0.2585	0.0051	0.0354	0.0006	237.1	46.3	233.5	4.1	224.1	3.9
HNGDM-4-6	720.8	987.5	0.7	0.0516	0.0012	0.2638	0.0058	0.0354	0.0006	268.4	50.7	237.7	4.7	224.5	3.9
HNGDM-4-17	983.8	1,615.5	0.6	0.0585	0.0012	0.2952	0.0056	0.0355	0.0006	547.5	42.5	262.7	4.4	225.0	3.9
HNGDM-4-5	2013.5	1880.7	1.1	0.0506	0.001	0.2523	0.0047	0.0356	0.0006	222.6	44.4	228.4	3.8	225.4	3.9
HNGDM-4-26	721.1	1861.7	0.4	0.0484	0.001	0.254	0.005	0.0357	0.0006	120.5	47.2	229.8	4.0	225.9	3.9
HNGDM-4-21	506.3	653.9	0.8	0.0508	0.0011	0.2531	0.0054	0.0358	0.0006	232.2	49.7	229.1	4.4	226.4	3.9
HNGDM-4-27	598.2	579.3	1.0	0.0525	0.0011	0.2519	0.005	0.0358	0.0006	306.6	45.8	228.1	4.0	227.0	3.9
HNGDM-4-18	709	856	0.8	0.0508	0.0011	0.249	0.005	0.0359	0.0006	233.0	47.3	225.7	4.1	227.5	3.9
HNGDM-4-16	1,000.4	1,398.4	0.7	0.052	0.001	0.2642	0.005	0.0359	0.0006	287.2	44.7	238.1	4.0	227.6	3.9
HNGDM-4-10	3,675.8	1989.1	1.8	0.0491	0.001	0.2512	0.0049	0.036	0.0006	153.9	46.9	227.6	4.0	227.9	3.9
HNGDM-4-29	1,426.7	783.5	1.8	0.0484	0.0013	0.258	0.0068	0.0361	0.0007	118.2	61.0	233.0	5.5	228.9	4.1
HNGDM-4-8	1749.1	3,724.7	0.5	0.0511	0.001	0.2548	0.0047	0.0364	0.0006	244.9	44.0	230.5	3.8	230.5	4.0
HNGDM-4-30	265.2	317.9	0.8	0.049	0.0011	0.2452	0.0053	0.0373	0.0007	149.2	50.9	222.6	4.3	236.1	4.1
HNGDM-2_1	310.0	446.6	0.7	0.0497	0.0011	0.2466	0.0053	0.0356	0.0006	181.0	50.4	223.8	4.3	225.2	3.9
HNGDM-2_2	416.1	594.6	0.7	0.0499	0.0010	0.2454	0.0048	0.0355	0.0006	192.3	46.6	222.8	3.9	225.1	3.9
HNGDM-2_3	537.5	792.9	0.7	0.0495	0.0010	0.2519	0.0048	0.0358	0.0006	171.5	45.9	228.1	3.9	226.5	3.9
HNGDM-2_4	545.5	772.1	0.7	0.0515	0.0010	0.2704	0.0052	0.0390	0.0007	263.9	45.3	243.0	4.1	246.5	4.2
HNGDM-2_5	872.6	1,561.3	0.6	0.0524	0.0011	0.2514	0.0053	0.0359	0.0006	302.0	48.7	227.7	4.3	227.5	3.9
HNGDM-2_6	515.9	810.9	0.6	0.0497	0.0010	0.2494	0.0047	0.0360	0.0006	179.4	45.4	226.0	3.8	227.9	3.9
HNGDM-2_7	1,064.8	1,468.5	0.7	0.0523	0.0010	0.2537	0.0047	0.0354	0.0006	300.3	44.0	229.6	3.8	224.4	3.8
HNGDM-2_8	751.0	1,107.6	0.7	0.0491	0.0010	0.2500	0.0047	0.0349	0.0006	152.4	45.2	226.5	3.8	221.2	3.8
HNGDM-2_9	658.9	953.0	0.7	0.0509	0.0010	0.2537	0.0047	0.0359	0.0006	237.6	44.1	229.5	3.8	227.3	3.9

TABLE 1 (*Continued*) LA–ICP–MS U–Pb analysis results of the Guandimiao batholith.

Spot	WB/10⁻⁶			Isotope ratio (± 1σ)						Isotope age (Ma) (± 1σ)					
	Th	U	Th/U	$^{207}Pb/^{206}Pb$		$^{207}Pb/^{235}U$		$^{206}Pb/^{238}U$		$^{207}Pb/^{206}Pb$		$^{207}Pb/^{235}U$		$^{206}Pb/^{238}U$	
				Ratio	Erro	Ratio	Erro	Ratio	Erro	Age	Erro	Age	Erro	Age	Erro
HNGDM-2_10	381.6	556.1	0.7	0.0513	0.0010	0.2531	0.0049	0.0357	0.0006	256.0	45.7	229.1	4.0	225.9	3.9
HNGDM-2_11	490.5	788.6	0.6	0.0505	0.0010	0.2511	0.0048	0.0350	0.0006	216.9	45.9	227.5	3.9	221.7	3.8
HNGDM-2_12	567.9	841.1	0.7	0.0502	0.0010	0.2520	0.0049	0.0353	0.0006	203.0	46.5	228.2	4.0	223.3	3.8
HNGDM-2_13	588.5	851.8	0.7	0.0509	0.0010	0.2530	0.0049	0.0363	0.0006	234.1	45.8	229.0	4.0	229.6	3.9
HNGDM-2_14	272.9	437.4	0.6	0.0512	0.0011	0.2537	0.0050	0.0356	0.0006	249.1	46.6	229.6	4.1	225.4	3.9
HNGDM-2_15	720.9	918.6	0.8	0.0528	0.0010	0.2471	0.0046	0.0351	0.0006	319.7	43.5	224.2	3.7	222.5	3.8
HNGDM-2_16	666.3	969.3	0.7	0.0498	0.0010	0.2457	0.0047	0.0359	0.0006	185.6	45.7	223.0	3.8	227.6	3.9
HNGDM-2_17	564.8	847.6	0.7	0.0520	0.0010	0.2537	0.0048	0.0356	0.0006	283.0	45.0	229.6	3.9	225.5	3.9
HNGDM-2_18	813.5	1,077.1	0.8	0.0698	0.0014	0.3426	0.0065	0.0351	0.0006	923.2	40.0	299.1	4.9	222.1	3.8
HNGDM-2_19	508.7	760.4	0.7	0.0517	0.0010	0.2510	0.0048	0.0351	0.0006	274.0	44.8	227.4	3.9	222.3	3.8
HNGDM-2_20	746.3	1,074.5	0.7	0.0512	0.0010	0.2504	0.0047	0.0354	0.0006	249.4	44.8	226.9	3.8	224.3	3.9
HNGDM-2_21	445.1	709.9	0.6	0.0508	0.0010	0.2533	0.0050	0.0358	0.0006	229.7	46.7	229.3	4.1	226.9	3.9
HNGDM-2_22	1,072.0	1,642.6	0.7	0.0505	0.0011	0.2460	0.0049	0.0334	0.0006	218.2	47.3	223.3	4.0	212.0	3.7
HNGDM-2_23	565.7	832.6	0.7	0.0482	0.0010	0.2454	0.0047	0.0359	0.0006	107.6	46.5	222.8	3.8	227.2	3.9
HNGDM-2_24	415.7	612.5	0.7	0.0558	0.0011	0.2750	0.0053	0.0352	0.0006	442.1	43.7	246.7	4.2	223.1	3.8
HNGDM-2_25	585.9	1,009.9	0.6	0.0512	0.0010	0.2526	0.0049	0.0350	0.0006	248.1	45.5	228.7	3.9	221.4	3.8
HNGDM-2_26	837.9	1,075.1	0.8	0.0686	0.0014	0.3450	0.0067	0.0361	0.0006	885.8	40.9	301.0	5.0	228.8	3.9
HNGDM-2_27	806.2	1,037.7	0.8	0.0502	0.0011	0.2545	0.0052	0.0355	0.0006	202.5	48.5	230.2	4.2	225.0	3.9
HNGDM-2_28	858.1	1,515.8	0.6	0.0504	0.0011	0.2475	0.0053	0.0353	0.0006	212.3	49.8	224.5	4.3	223.8	3.9
HNGDM-2_29	580.5	835.9	0.7	0.0641	0.0014	0.3372	0.0071	0.0372	0.0007	745.3	44.9	295.1	5.4	235.4	4.1
HNGDM-2_30	340.1	545.4	0.6	0.0497	0.0010	0.2434	0.0048	0.0357	0.0006	180.5	47.3	221.2	3.9	226.1	3.9
L4															
HNGDM-6_1	993.7	489.9	2.0	0.0722	0.0015	0.5501	0.0117	0.0547	0.0010	992.5	41.8	445.1	7.6	343.0	6.0
HNGDM-6_2	497.2	365.1	1.4	0.1614	0.0030	10.1749	0.1946	0.4618	0.0082	2,470.1	31.2	2,450.8	17.7	2,447.3	36.1
HNGDM-6_3	2,593.4	857.9	3.0	0.0526	0.0011	0.2543	0.0055	0.0353	0.0006	309.5	48.3	230.1	4.4	223.7	4.0
HNGDM-6_4	836.0	574.9	1.5	0.0491	0.0010	0.2441	0.0050	0.0356	0.0006	150.2	47.3	221.8	4.0	225.2	4.0
HNGDM-6_5	130.7	88.2	1.5	0.1109	0.0021	4.9884	0.1042	0.3248	0.0058	1813.5	34.4	1817.4	17.7	1813.0	28.2
HNGDM-6_6	1,536.0	889.9	1.7	0.0655	0.0013	0.3494	0.0067	0.0380	0.0007	790.0	40.0	304.3	5.0	240.6	4.2
HNGDM-6_7	1,024.9	1,110.3	0.9	0.0495	0.0011	0.2523	0.0054	0.0360	0.0007	172.0	49.3	228.4	4.4	227.8	4.0
HNGDM-6_8	717.5	555.0	1.3	0.0505	0.0012	0.1388	0.0034	0.0201	0.0004	215.9	56.0	132.0	3.0	128.5	2.3
HNGDM-6_9	61.5	471.4	0.1	0.0717	0.0014	1.6530	0.0333	0.1671	0.0030	976.6	39.0	990.7	12.7	996.0	16.5
HNGDM-6_10	307.4	364.8	0.8	0.0503	0.0012	0.2453	0.0061	0.0352	0.0007	210.9	56.1	222.8	5.0	222.7	4.0
HNGDM-6_11	1,348.3	1,195.2	1.1	0.0521	0.0011	0.1468	0.0032	0.0210	0.0004	288.3	49.3	139.1	2.8	133.8	2.4
HNGDM-6_12	87.9	51.0	1.7	0.0568	0.0019	0.5433	0.0198	0.0699	0.0014	483.5	73.1	440.6	13.0	435.7	8.3
HNGDM-6_13	114.9	142.7	0.8	0.1087	0.0021	4.4792	0.0901	0.3034	0.0054	1777.6	34.3	1727.1	16.7	1708.1	26.8
HNGDM-6_14	44.2	96.6	0.5	0.1455	0.0028	8.0333	0.1736	0.4139	0.0074	2,293.6	32.4	2,234.8	19.5	2,232.7	33.9
HNGDM-6_15	38.0	22.3	1.7	0.0582	0.0027	0.5428	0.0273	0.0690	0.0015	535.8	97.6	440.3	18.0	430.3	9.3
HNGDM-6_16	171.8	997.2	0.2	0.1320	0.0025	6.6136	0.1232	0.3494	0.0062	2,124.3	32.3	2061.2	16.4	1931.6	29.7
HNGDM-6_17	530.3	512.1	1.0	0.0473	0.0012	0.1133	0.0028	0.0166	0.0003	61.6	58.7	108.9	2.6	106.0	1.9
HNGDM-6_18	35.1	28.6	1.2	0.0558	0.0022	0.5013	0.0215	0.0649	0.0014	442.3	85.7	412.6	14.5	405.3	8.2
HNGDM-6_19	90.8	434.7	0.2	0.1159	0.0022	5.3244	0.1019	0.3310	0.0059	1893.7	33.3	1872.8	16.4	1843.0	28.6
HNGDM-6_20	569.7	354.3	1.6	0.0665	0.0013	0.6790	0.0138	0.0736	0.0013	822.5	41.0	526.1	8.4	457.7	8.0
HNGDM-8_25	324.4	249.8	1.3	0.0491	0.0012	0.1335	0.0033	0.0198	0.0004	153.0	56.5	127.2	2.9	126.5	2.3
HNGDM-8_14	724.9	948.0	0.8	0.0500	0.0011	0.2348	0.0052	0.0339	0.0006	194.2	50.1	214.1	4.2	214.7	3.8
HNGDM-8_16	1,064.2	1,426.6	0.7	0.0471	0.0010	0.2501	0.0050	0.0348	0.0006	55.1	47.8	226.7	4.1	220.7	3.9
HNGDM-8_4	999.2	860.3	1.2	0.0503	0.0011	0.2480	0.0055	0.0349	0.0006	210.2	50.2	224.9	4.5	221.1	3.9
HNGDM-8_6	282.6	395.6	0.7	0.0513	0.0011	0.2514	0.0054	0.0355	0.0006	254.9	48.8	227.7	4.4	225.1	4.0
HNGDM-8_5	171.6	109.7	1.6	0.0551	0.0014	0.5145	0.0135	0.0658	0.0012	415.9	53.8	421.5	9.1	411.0	7.4
HNGDM-8_1	316.5	262.4	1.2	0.0531	0.0011	0.5303	0.0117	0.0697	0.0013	331.7	47.5	432.0	7.8	434.3	7.6

TABLE 1 (*Continued*) LA–ICP–MS U–Pb analysis results of the Guandimiao batholith.

Spot	WB/10⁻⁶			Isotope ratio (± 1σ)						Isotope age (Ma) (± 1σ)					
	Th	U	Th/U	²⁰⁷Pb/²⁰⁶Pb		²⁰⁷Pb/²³⁵U		²⁰⁶Pb/²³⁸U		²⁰⁷Pb/²⁰⁶Pb		²⁰⁷Pb/²³⁵U		²⁰⁶Pb/²³⁸U	
				Ratio	Erro	Ratio	Erro	Ratio	Erro	Age	Erro	Age	Erro	Age	Erro
HNGDM-8_18	593.6	595.3	1.0	0.0574	0.0011	0.5653	0.0113	0.0730	0.0013	505.0	43.4	455.0	7.3	454.5	7.8
HNGDM-8_21	83.3	107.8	0.8	0.0731	0.0016	0.7755	0.0183	0.0751	0.0014	1,015.3	43.9	582.9	10.5	466.8	8.2
HNGDM-8_9	15.6	423.7	0.0	0.0580	0.0012	0.6880	0.0155	0.0872	0.0016	530.3	46.6	531.6	9.3	539.1	9.4
HNGDM-8_13	594.1	328.2	1.8	0.1926	0.0036	2.6082	0.0498	0.1002	0.0018	2,764.5	30.6	1,303.0	14.0	615.4	10.5
HNGDM-8_27	224.0	84.9	2.6	0.0639	0.0013	1.1044	0.0242	0.1268	0.0023	739.7	42.9	755.5	11.7	769.7	13.1
HNGDM-8_19	100.0	76.7	1.3	0.0652	0.0014	1.1749	0.0275	0.1300	0.0024	779.2	44.4	788.9	12.9	787.6	13.4
HNGDM-8_20	98.3	56.1	1.8	0.0655	0.0015	1.1685	0.0308	0.1302	0.0024	791.8	48.0	785.9	14.4	789.0	13.7
HNGDM-8_3	315.1	240.0	1.3	0.0671	0.0013	1.2193	0.0245	0.1331	0.0024	841.4	40.0	809.4	11.2	805.7	13.5
HNGDM-8_24	170.0	181.2	0.9	0.0718	0.0014	1.6238	0.0327	0.1628	0.0029	979.0	38.9	979.4	12.7	972.4	16.1
HNGDM-8_28	204.7	214.6	1.0	0.0716	0.0014	1.6213	0.0316	0.1648	0.0029	973.7	38.4	978.5	12.2	983.3	16.2
HNGDM-8_23	120.7	104.2	1.2	0.0732	0.0015	1.7371	0.0416	0.1728	0.0031	1,020.7	41.9	1,022.4	15.4	1,027.8	17.2
HNGDM-8_8	45.8	104.5	0.4	0.0734	0.0015	1.7924	0.0384	0.1763	0.0032	1,023.8	39.6	1,042.7	14.0	1,046.8	17.3
HNGDM-8_2	44.7	644.4	0.1	0.0707	0.0013	1.7358	0.0324	0.1781	0.0032	949.9	37.8	1,021.9	12.0	1,056.5	17.3
HNGDM-8_12	147.2	121.0	1.2	0.0752	0.0015	1.8512	0.0383	0.1812	0.0032	1,073.4	38.6	1,063.8	13.6	1,073.4	17.7
HNGDM-8_22	366.3	358.4	1.0	0.0752	0.0014	1.8625	0.0355	0.1817	0.0032	1,074.1	37.4	1,067.9	12.6	1,076.2	17.6
HNGDM-8_26	49.5	85.6	0.6	0.0762	0.0015	1.9287	0.0401	0.1855	0.0033	1,099.6	38.6	1,091.1	13.9	1,096.9	18.0
HNGDM-8_11	116.2	222.4	0.5	0.0787	0.0015	2.0323	0.0399	0.1925	0.0034	1,164.2	37.2	1,126.4	13.4	1,135.0	18.5
HNGDM-8_29	17.2	715.5	0.0	0.0989	0.0018	3.9441	0.0723	0.2869	0.0051	1,602.6	34.2	1,622.8	14.8	1,625.9	25.4
HNGDM-8_30	128.3	303.0	0.4	0.1071	0.0020	4.5705	0.0859	0.3060	0.0054	1751.0	33.7	1743.9	15.7	1720.8	26.8
HNGDM-8_10	102.8	247.7	0.4	0.1114	0.0021	4.9857	0.0956	0.3279	0.0058	1822.7	33.4	1816.9	16.2	1828.3	28.2
HNGDM-8_7	177.6	262.2	0.7	0.1373	0.0026	7.1652	0.1440	0.3898	0.0069	2,193.4	32.2	2,132.2	17.9	2,121.7	32.1
HNGDM-8_15	75.4	77.4	1.0	0.1732	0.0033	11.4801	0.2406	0.4906	0.0087	2,588.6	30.9	2,563.0	19.6	2,573.1	37.8
HNGDM_1	193.06	334.74	0.6	0.06303	0.00238	0.09244	0.00144	0.7656	0.03605	709.1	78.2	569.9	8.5	577.2	20.7
HNGDM_2	559.10	1,297.83	0.4	0.052	0.0008	0.04191	0.0004	0.302	0.00483	285.4	34.9	264.7	2.5	268.0	3.8
HNGDM_3	99.28	149.70	0.7	0.12814	0.00147	0.38748	0.00361	7.02383	0.13113	2072.6	20.1	2,111.1	16.8	2,114.4	16.6
HNGDM_4	559.64	633.11	0.9	0.05435	0.00099	0.04637	0.00046	0.33833	0.00654	385.6	40.4	292.2	2.9	295.9	5.0
HNGDM_5	130.33	569.94	0.2	0.05512	0.00127	0.05993	0.00066	0.45338	0.0117	417.1	50.1	375.2	4.0	379.6	8.2
HNGDM_6	530.01	1,487.06	0.4	0.05334	0.00118	0.04098	0.00044	0.29027	0.00684	343.2	49.5	258.9	2.7	258.8	5.4
HNGDM_7	141.99	315.41	0.5	0.1715	0.00177	0.4839	0.00434	11.36067	0.17068	2,572.3	17.1	2,544.2	18.9	2,553.2	14.0
HNGDM_8	1,286.32	2071.90	0.6	0.1525	0.00163	0.06103	0.00055	1.29337	0.01432	2,374.1	18.1	381.9	3.3	842.8	6.3
HNGDM_9	742.85	1,479.61	0.5	0.06991	0.00133	0.04399	0.00046	0.42958	0.00886	925.8	38.5	277.5	2.9	362.9	6.3
HNGDM_10	1,678.17	822.21	2.0	0.05867	0.00246	0.03881	0.00063	0.27666	0.0124	554.9	89.0	245.5	3.9	248.0	9.9
HNGDM_11	731.74	1,115.60	0.7	0.05709	0.00072	0.07161	0.00065	0.55765	0.00742	494.4	27.9	445.9	3.9	450.0	4.8
HNGDM_12	480.04	854.75	0.6	0.05424	0.00161	0.04701	0.00059	0.35031	0.01142	380.9	65.4	296.2	3.7	305.0	8.6
G3															
HNGDM07-2_1	287.1	651.9	0.44	0.0523	0.0012	0.2625	0.0052	0.0364	0.0006	298.6	50.1	236.7	4.2	230.5	4.0
HNGDM07-2_2	144.9	2,333.5	0.06	0.0518	0.0011	0.2585	0.0049	0.0362	0.0006	277.4	48.4	233.5	3.9	229.1	4.0
HNGDM07-2_3	127.1	1,165.1	0.11	0.0506	0.0011	0.2507	0.0048	0.0360	0.0006	220.6	49.5	227.1	3.9	227.8	3.9
HNGDM07-2_4	686.2	3,309.6	0.21	0.0528	0.0011	0.2627	0.0050	0.0361	0.0006	322.1	47.9	236.9	4.0	228.4	3.9
HNGDM07-2_5	610.5	1,058.9	0.58	0.0509	0.0011	0.2597	0.0050	0.0370	0.0007	234.3	49.9	234.4	4.1	234.4	4.1
HNGDM07-2_6	800.5	519.1	1.54	0.0524	0.0012	0.2629	0.0056	0.0364	0.0007	301.7	52.8	237.0	4.5	230.6	4.0
HNGDM07-2_7	1,372.0	988.9	1.39	0.0866	0.0019	0.4325	0.0083	0.0362	0.0006	1,350.7	41.4	364.9	5.9	229.5	4.0
HNGDM07-2_8	876.2	1,099.3	0.80	0.0955	0.0021	0.4936	0.0095	0.0375	0.0007	1,537.4	40.6	407.4	6.5	237.3	4.1
HNGDM07-2_9	2,596.6	2,199.6	1.18	0.0663	0.0014	0.3267	0.0062	0.0357	0.0006	815.9	44.7	287.0	4.8	226.3	3.9
HNGDM07-2_10	2,112.1	2029.5	1.04	0.0691	0.0015	0.3422	0.0065	0.0359	0.0006	902.6	44.0	298.8	4.9	227.4	3.9
HNGDM07-2_11	486.7	599.4	0.81	0.0531	0.0012	0.2647	0.0054	0.0362	0.0006	331.5	51.3	238.5	4.4	229.1	4.0
HNGDM07-2_12	1997.0	2,219.6	0.90	0.0924	0.0020	0.4624	0.0089	0.0363	0.0006	1,474.5	40.8	385.9	6.1	229.9	4.0
HNGDM07-2_13	455.2	743.9	0.61	0.0518	0.0012	0.2585	0.0051	0.0362	0.0006	277.0	50.4	233.4	4.1	229.1	4.0
HNGDM07-2_14	2,147.5	998.5	2.15	0.0517	0.0012	0.2542	0.0050	0.0357	0.0006	271.2	50.2	230.0	4.1	226.0	3.9

TABLE 1 (*Continued*) LA−ICP−MS U−Pb analysis results of the Guandimiao batholith.

Spot	WB/10⁻⁶			Isotope ratio (± 1σ)						Isotope age (Ma) (± 1σ)					
	Th	U	Th/U	$^{207}Pb/^{206}Pb$		$^{207}Pb/^{235}U$		$^{206}Pb/^{238}U$		$^{207}Pb/^{206}Pb$		$^{207}Pb/^{235}U$		$^{206}Pb/^{238}U$	
				Ratio	Erro	Ratio	Erro	Ratio	Erro	Age	Erro	Age	Erro	Age	Erro
HNGDM07-2_15	6,116.0	2,551.7	2.40	0.0623	0.0014	0.2975	0.0057	0.0346	0.0006	684.1	45.9	264.4	4.5	219.5	3.8
HNGDM07-2_16	219.4	1,309.9	0.17	0.0515	0.0022	0.2278	0.0092	0.0321	0.0007	261.6	95.2	208.4	7.6	203.7	4.2
HNGDM07-2_17	470.9	1,055.5	0.45	0.0509	0.0012	0.2340	0.0047	0.0333	0.0006	236.8	51.3	213.5	3.9	211.4	3.7
HNGDM07-2_18	168.2	516.0	0.33	0.0520	0.0012	0.2600	0.0055	0.0363	0.0007	285.8	53.3	234.7	4.4	229.6	4.0
HNGDM07-2_19	441.6	1,458.4	0.30	0.0521	0.0012	0.2603	0.0051	0.0363	0.0006	288.8	49.6	234.9	4.1	229.5	4.0
HNGDM07-2_20	4,728.7	3,022.5	1.56	0.0908	0.0020	0.3737	0.0072	0.0299	0.0005	1,441.4	41.1	322.4	5.3	189.7	3.3
HNGDM07-2_21	828.7	1,473.1	0.56	0.0513	0.0011	0.2616	0.0052	0.0370	0.0007	253.4	50.5	235.9	4.2	234.2	4.1
HNGDM07-2_22	786.1	1,018.4	0.77	0.1583	0.0035	0.7949	0.0156	0.0364	0.0007	2,437.4	37.2	593.9	8.8	230.6	4.0
HNGDM07-2_23	1771.3	1,541.0	1.15	0.0512	0.0015	0.2525	0.0069	0.0358	0.0007	249.3	67.2	228.6	5.6	226.6	4.2
HNGDM07-2_24	307.6	706.0	0.44	0.0675	0.0016	0.3354	0.0072	0.0360	0.0007	854.4	49.0	293.7	5.5	228.1	4.0
HNGDM07-2_25	682.8	1,490.8	0.46	0.0518	0.0012	0.2573	0.0054	0.0360	0.0006	278.1	52.4	232.5	4.3	228.0	4.0
HNGDM07-2_26	388.6	747.8	0.52	0.0517	0.0012	0.2593	0.0053	0.0364	0.0007	272.8	51.7	234.1	4.3	230.3	4.0
HNGDM07-2_27	602.2	1787.8	0.34	0.0516	0.0012	0.2570	0.0052	0.0361	0.0006	268.4	51.3	232.2	4.2	228.7	4.0
HNGDM07-2_28	564.6	698.6	0.81	0.0511	0.0012	0.2547	0.0053	0.0362	0.0006	245.4	53.0	230.4	4.3	228.9	4.0
HNGDM07-2_29	1,082.0	772.8	1.40	0.0522	0.0012	0.2605	0.0054	0.0362	0.0006	294.3	52.1	235.0	4.4	229.1	4.0
HNGDM07-2_30	394.9	765.6	0.52	0.0517	0.0012	0.2597	0.0055	0.0365	0.0007	270.0	53.1	234.4	4.4	230.9	4.0

depletion and Th, U, La, Ce, Nd, and Hf enrichment (Figure 7C). The chondrite-normalized REE patterns of G1 and G2-1 are similar (Figure 7D), exhibiting negative slopes with strong light-heavy rare earth element fractionation [$(La/Yb)_N$ = 14.75–19.21; LREE/HREE = 12.00–14.08] and negative Eu anomalies (Eu/Eu* = 0.44–0.51). G1 and G2-1 have low Rb/Sr ratios (1.71–2.80) and high K/Rb ratios (136–155). However, G2-2 and G-3 have relatively higher Rb/Sr ratios (10.5–14.19) and lower K/Rb ratios (71.09–117). All granitic samples have Zr + Nb + Ce + Y values from 124.3 to 295.7 ppm, and the 10000 × Ga/Al ranges from 2.09 to 3.02, which is lower than the boundary value of 2.6 for A-type granite (Whalen et al., 1987),.

5.3 Sr−Nd−Pb isotopes

The $\varepsilon_{Nd}(t)$ values were calculated at 226–224 Ma for G2-1, 227–225 Ma for G2-2, 239 Ma for G1, 190 Ma for the granite porphyry and 121 Ma for L4 on the basis of zircon U-Pb dating. The Sr-Nd-Pb isotope compositions of the rocks from the Guandimiao batholith are shown in Table 3. The $^{87}Rb/^{86}Sr$ ratios of the Guandimiao batholith range from 7.95 to 8.74, and the calculated ISr values range from 7.1229 to 7.1796 (G2-2 and G3 have high $^{87}Rb/^{86}Sr$ ratios, indicating that the calculated results cannot represent the actual isotopic compositions). The $^{87}Rb/^{86}Sr$ ratios of L4 range from 0.11 to 0.38, and the calculated ISr values range from 0.71449 to 0.71748. The calculated $\varepsilon_{Nd}(t)$ values are −9.37 to −10.54 for G2-1, −6.95 for G1 and −12.14 for G2-2. The $^{143}Nd/^{144}Nd$ ratios and calculated $\varepsilon_{Nd}(t)$ values are

0.512558 and −8.96 for G3 and 0.512042–0.512071 and −10.18 to −9.62 for L4, respectively. Since the $f_{Sm/Nd}$ of the samples deviates from the mean value for continental crust, a two-stage model is used. Thus, we obtain two stages of depleted mantle model ages (T_{DM2}) based on the model reported by Depaolo (1981). The calculated two-stage model ages are 1859–1764 Ma for G2-1, 1,568 Ma for G1, 1730 Ma for G2-1, 1928 Ma for G3 and 1,577–1,435 Ma for L4.

The $^{206}Pb/^{204}Pb$, $^{207}Pb/^{204}Pb$, and $^{208}Pb/^{204}Pb$ ratios of G2-1 vary from 18.821 to 18.611, 15.707–15.712, and 38.977–39.056, respectively. For G1, the $^{206}Pb/^{204}Pb$ ratio is 18.707, the $^{207}Pb/^{204}Pb$ ratio is 15.71, and the $^{208}Pb/^{204}Pb$ ratio is 39.109. For G2-2, the $^{206}Pb/^{204}Pb$ ratio is 18.701, the $^{207}Pb/^{204}Pb$ ratio is 15.701, and the $^{208}Pb/^{204}Pb$ ratio is 38.887. For G3, the $^{206}Pb/^{204}Pb$ ratio is 19.21, the $^{207}Pb/^{204}Pb$ ratio is 15.738, and the $^{208}Pb/^{204}Pb$ ratio is 39.081. For L4, the $^{206}Pb/^{204}Pb$ ratio is 18.95–19.96, the $^{207}Pb/^{204}Pb$ ratio is 15.71–15.78, and the $^{208}Pb/^{204}Pb$ ratio is 39.87–43.090. These data reflect relatively uniform Pb isotope ratios. The initial Pb isotope ratios of the samples were calculated using the formulas of Hart (1984). The calculated results for $(^{206}Pb/^{204}Pb)_i$, $(^{207}Pb/^{204}Pb)_i$, and $(^{208}Pb/^{204}Pb)_i$ range from 17.875 to 18.113, 15.664–15.682, and 37.75–37.787, respectively, for G2-1. For G1, the $(^{206}Pb/^{204}Pb)_i$ ratio is 18.36, the $(^{207}Pb/^{204}Pb)_i$ ratio is 15.692, and the $(^{208}Pb/^{204}Pb)_i$ ratio is 38.613. For G2-2, the $(^{206}Pb/^{204}Pb)_i$ ratio is 17.662, the $(^{207}Pb/^{204}Pb)_i$ ratio is 15.648, and the $(^{208}Pb/^{204}Pb)_i$ ratio is 36.992. For G3, the $(^{206}Pb/^{204}Pb)_i$ ratio is 18.588, the $(^{207}Pb/^{204}Pb)_i$ ratio is 15.707, and the $(^{208}Pb/^{204}Pb)_i$ ratio is 38.57. For L4, the $(^{206}Pb/^{204}Pb)_i$ ratios range from 18.31 to 19.72, the $(^{207}Pb/^{204}Pb)_i$ ratios range from

TABLE 2 Whole-rock geochemical results of igneous rocks in Guandimiao batholith.

Sample	HNGDM2-1	HNGDM-3	HNGDM-3-1	HNGDM-4	HNGDM-4-1	HNGDM-5-1	HNGDM-2	HNGDM07-2	HNGDM-6	HNGDM-6-1	HNGDM-6-2	HNGDM-7
	G1	G2-1		G2-2			G3			L4		
SiO2	69.3	70.1	69.8	67.9	67.3	76.7	74.1	75.2	55.9	55.4	56.3	57.1
TiO2	0.39	0.41	0.39	0.42	0.43	0.12	0.15	0.15	1.22	1.21	1.23	1.07
Al2O3	14.6	14.6	14.4	14.7	14.6	12.6	14.4	14.4	16.6	16.4	17.0	12.8
Fe2O3	0.94	2.43	1.79	0.56	0.81	0.21	0.93	1.63	3.18	2.82	4.96	1.34
FeO	1.89	0.70	1.15	2.62	2.68	1.01	0.56	0.69	4.35	4.53	2.85	5.45
MnO	0.07	0.07	0.07	0.10	0.11	0.06	0.05	0.06	0.20	0.19	0.21	0.21
MgO	1.58	1.09	1.19	1.44	1.47	0.31	0.44	0.39	5.00	5.08	4.99	7.19
CaO	2.70	0.44	1.93	2.58	2.23	0.37	0.41	0.26	2.01	2.25	0.80	3.62
Na2O	3.22	3.19	2.51	4.95	4.12	2.79	3.08	2.41	5.37	5.40	6.07	4.01
K2O	4.05	4.57	4.57	3.39	4.41	4.84	4.22	4.02	1.01	0.92	0.63	0.11
P2O5	0.10	0.16	0.14	0.14	0.13	0.15	0.13	0.12	0.33	0.35	0.34	0.49
CO2	0.30	0.18	0.22	1.85	1.16	0.35	0.55	0.3	1.53	1.89	0.31	2.40
H2O+	1.08	2.24	1.86	1.00	1.26	0.80	1.26	1.54	3.18	3.84	4.58	4.54
LOI	0.63	2.07	1.67	2.93	1.96	0.73	1.33	1.82	4.55	5.13	4.25	5.91
SUM	99.5	99.8	99.6	102	100	99.9	99.8	101	99.9	100	100	100
Na2O + K2O	7.27	7.76	7.08	8.34	8.53	7.63	7.30	6.43	6.38	6.32	6.70	4.12
K2O/Na2O	1.26	1.43	1.82	0.69	1.07	1.73	1.37	1.67	0.19	0.17	0.10	0.03
A/CNK	1.00	1.32	1.14	0.89	0.94	1.19	1.38	1.61	1.10	1.05	1.34	0.80
A/NK	1.51	1.43	1.58	1.24	1.26	1.28	1.49	1.73	1.67	1.66	1.60	1.91
Fe/Mg	1.73	2.65	2.32	2.17	2.32	3.87	3.17	5.53	1.44	1.39	1.47	0.93
Li	73.9	47.7	63.8	75.90	80.70	63.60	34.80	32.0	64.2	72.5	72.1	72.4
Be	4.87	6.36	5.80	5.24	3.57	3.67	7.51	5.88	3.36	3.64	3.02	3.20
Co	9.01	7.61	7.41	8.87	9.60	1.63	1.69	1.86	33.2	30.2	30.8	38.4
Ni	24.90	19.40	18.40	21.60	21.60	2.07	2.96	3.72	131	85.7	135	274
Cu	20.40	32.80	36.20	7.73	16.50	2.94	20.10	24.8	47.8	33.3	42.4	12.6
Zn	44.30	116.00	68.30	56.60	63.60	67.70	40.40	58.1	108	94.6	96.6	111
Ga	18.60	18.90	15.90	19.10	18.80	17.90	23.00	24.0	17.5	17.4	17.9	19.3
Rb	253.00	268.00	278.00	386.00	242.00	352.00	441.00	427	53.6	45.7	31.6	6.81
Sr	148.00	97.90	134.00	138.00	93.90	33.40	41.60	30.1	408	318	583	177
Mo	0.31	0.43	0.25	13.80	1.13	1.89	0.24	0.67	0.46	0.30	0.32	0.38
Cd	0.06	0.40	0.21	0.08	<0.05	0.12	0.06	0.08	0.12	0.12	0.06	<0.05
In	<0.05	<0.05	<0.05	0.05	<0.05	0.05	<0.05	<0.05	0.06	0.05	0.06	0.06

(Continued on following page)

TABLE 2 (*Continued*) Whole-rock geochemical results of igneous rocks in Guandimiao batholith.

Sample	HNGDM2-1	HNGDM-3	HNGDM-3-1	HNGDM-4	HNGDM-4-1	HNGDM-5-1	HNGDM-2	HNGDM07-2	HNGDM-6	HNGDM-6-1	HNGDM-6-2	HNGDM-7
	G1	G2-1		G2-2			G3			L4		
Cs	22.00	19.10	18.00	17.50	10.80	35.90	60.70	47.9	6.70	6.47	2.50	0.63
Ba	435.00	628.00	546.00	626.00	459.00	208.00	196.00	189	487	455	522	326
Tl	1.38	1.62	1.65	2.40	1.50	1.98	2.25	2.01	0.29	0.25	0.20	<0.05
Pb	44.70	46.20	37.30	50.10	46.30	50.80	24.30	25.3	16.4	13.7	10.2	12.7
Bi	1.19	0.96	0.98	1.79	0.82	5.94	0.99	2.31	0.17	0.13	0.13	0.14
Th	28.00	26.50	31.20	31.40	33.30	20.10	24.20	22.4	32.70	34.80	35.80	71.00
U	6.37	10.90	5.15	6.83	5.90	9.12	9.66	7.57	6.29	6.35	6.68	9.52
Nb	12.4	13.1	12.2	13.8	12.6	16.2	18.3	18.1	31.6	33.5	32.8	25.8
Ta	1.72	1.70	1.46	1.89	1.65	3.81	3.43	3.35	2.23	2.37	2.43	1.65
Zr	72.8	124	114	183	121	52.9	66.0	81.8	181	183	186	359
Hf	3.11	5.11	4.86	6.52	5.08	2.78	3.38	2.92	6.03	6.28	6.65	13.5
W	6.33	11.4	45.7	2.91	1.42	4.08	5.16	8.76	3.74	3.84	4.03	5.69
V	51.5	43.2	39.8	50.0	43.6	7.44	15.6	10.5	188.0	188	186	171.0
La	30.9	35.4	41.5	40.6	43.3	21.0	19.7	22.6	26.7	29.8	33.0	67.6
Ce	63.0	67.2	80.5	80.8	86.7	43.3	40.6	48.6	67.4	68.7	70.8	161
Pr	6.80	7.50	9.16	8.73	9.29	4.88	4.77	5.48	6.96	8.06	8.37	19.8
Nd	23.7	27.6	33.6	32.4	33.8	17.5	17.3	19.4	28.4	33.7	36.4	81.6
Sm	4.34	4.93	6.19	5.79	6.08	4.02	3.78	4.34	5.01	5.92	6.18	13.0
Eu	0.74	0.64	0.87	0.87	0.82	0.29	0.24	0.23	1.05	1.33	1.42	2.73
Gd	3.26	3.78	4.82	4.24	4.32	3.36	3.08	3.35	3.50	4.24	4.81	7.30
Tb	0.50	0.60	0.72	0.65	0.67	0.51	0.49	0.57	0.53	0.65	0.70	0.91
Dy	2.80	3.17	3.68	3.43	3.42	2.67	2.74	3.06	3.18	4.02	4.13	4.46
Ho	0.56	0.61	0.74	0.66	0.64	0.43	0.49	0.53	0.65	0.83	0.88	0.87
Er	1.58	1.67	1.99	1.86	1.73	1.05	1.32	1.46	1.88	2.29	2.60	2.31
Tm	0.22	0.23	0.29	0.26	0.24	0.15	0.20	0.23	0.28	0.33	0.34	0.32
Yb	1.36	1.48	1.80	1.75	1.52	0.96	1.26	1.35	1.64	2.08	2.14	1.94
Lu	0.24	0.23	0.28	0.27	0.24	0.14	0.19	0.18	0.28	0.33	0.34	0.31
Y	14.8	16.4	18.2	18.1	16.8	11.9	13.1	15.6	16.4	20.7	24.1	22.6
Zr + Nb + Ce + Y	163	221	225	296	237	124	138	164				
10000×Ga/Al	2.41	2.45	2.09	2.32	2.43	2.69	3.02	3.14				
Rb/Sr	1.71	2.74	2.07	2.80	2.58	10.50	10.60	14.2				

TABLE 2 (Continued) Whole-rock geochemical results of igneous rocks in Guandimiao batholith.

Sample	HNGDM2-1	HNGDM-3	HNGDM-3-1	HNGDM-4	HNGDM-4-1	HNGDM-5-1	HNGDM-2	HNGDM07-2	HNGDM-6	HNGDM-6-1	HNGDM-6-2	HNGDM-7
	G1	G2-1		G2-2			G3			L4		
K/Rb	136	145	139	140	155	117	81.1	78.1				
ΣREE	140	155	186	182	193	100	96.2	127	164	183	196	387
LREE	129	143	172	169	180	91.0	86.4	100	136	148	156	346
HREE	10.5	11.8	14.3	13.1	12.80	9.30	9.77	26.3	28.3	35.5	40.0	41.0
LREE/HREE	12.3	12.2	12.0	12.9	14.1	9.8	8.84	3.82	4.78	4.16	3.90	8.43
LaN/YbN	16.3	17.2	16.5	16.6	20.4	15.7	11.2	28.7	27.9	24.5	26.4	59.7
δEu	0.58	0.44	0.47	0.51	0.47	0.23	0.21	0.18	0.73	0.77	0.77	0.78
δCe	1.02	0.96	0.97	1.00	1.01	1.01	1.00	1.02	1.17	1.05	1.00	1.05
TZr(°C)	714	785	764	771	743	713	739					

15.68 to 15.77, and the $(^{208}Pb/^{204}Pb)_i$ ratios range from 39.79 to 42.94. All analyzed Pb isotope compositions are shown in Table 4.

6 Discussion

6.1 Magmatism stages of the guandimiao batholith

Previous research on the biotite granodiorite of the Guandimiao batholith found that it formed 239 Ma (Wang et al., 2005a). The biotite monzogranite and two-mica monzogranite have a wide range of formation ages (230–220 Ma; Huang and Depaolo, 1989; Zhao et al., 2015). The Zhoujialing biotite granite exposed west of the Guandimiao batholith are formed at 208–203 Ma (Miao, 2014). Dai et al. (2008) determined that the formation age of lamprophyre was 153 Ma (Table 5).

In this study, high-precision LA-ICP-MS zircon U-Pb data were obtained for the Guandimiao batholith. The U-Pb data for G2-1 range from 225.9 ± 0.72 to 223.64 ± 1.33 Ma and for G2-2 from 227.5 ± 1.0 to 225.5 ± 2.2 Ma. These ages indicate that the main part of the batholith was formed in the Late Triassic. Due to the high emplacement and fast cooling of G3 and L4, the time was insufficient for the crystallization of sufficient zircon crystals. In addition, mafic magma is generally unsaturated silicon, and it is very hard to crystallize sufficient and well-formed zircon grains. In G3, two age groups were identified. The first group of ages yields a concordia U–Pb age of 229.37 ± 0.71 Ma, much closer to the main ages of the batholith within the allowed error range. These results suggest that the U-Pb ages of zircons were captured from G2-1 and G2-2. The second group of ages of zircons ranges from 189.7 to 211.4 Ma, which is significantly lower than those of G2-1 and G2-2. This more likely represents the crystallization age of G3. Four zircon grains in group one collected from lamprophyre formed 106.0 to 133.8 Ma and yield a concordia U-Pb age of 121.22 ± 1.16 Ma. However, the U-Pb ages of zircons from group two range from 217.7 to 2,573.1 Ma. Due to the same characteristics as those from felsic granite (G1, G2-1, G2-2, and G3) and the long-term temporal span, there is no doubt that it was from the succession of the source area or the capture crystals from the surrounding rocks.

Thus, four main stages of magmatism can be determined in the Guandimiao batholith: Stage 1 (G1; 239 Ma)→Stage 2 (G2-1, G2-2; 230–203 Ma)→Stage 3 (G3; 211–190 Ma)→Stage 4 (L4; 121 Ma) (Figure 8). Zhou et al. (2006) proposed that the formation ages of igneous rocks in the SCB contain two principal periods and five main stages. The Indosinian magmatism was between 251 and 205 Ma and can be divided into two stages (251–234 Ma and 234–205 Ma). The first stage formed 251–234 Ma and is defined as S-type granite with high aluminum contents. The 234–205 Ma stage was dominated by postcollisional granitoids without contemporaneous volcanic

TABLE 3 Sr-Nd isotopic compositions of igneous rocks in Guandimiao batholith.

Lithology	Rb	Sr	^{87}Rb	^{87}Sr	ISr	Sm	Nd	^{147}Sm	^{143}Nd	TDM	T2DM	εNd(t)	References
	(ppm)	(ppm)	^{86}Sr	^{86}Sr		(ppm)	(ppm)	^{144}Nd	^{144}Nd				
G1	253.00	148.00	4.95	0.73	0.71	4.34	23.70	0.11	0.51	1,427.00	1,518.00	−6.17	This paper
G3	441.00	41.60	30.95	0.80	0.73	3.78	17.30	0.13	0.51	2,234.00	1928.00	−12.14	
G2-1	268.00	97.90	7.95	0.74	0.72	4.93	27.60	0.11	0.51	1704.00	1859.00	−10.54	
	386.00	138.00	8.12	0.74	0.72	5.79	32.40	0.11	0.51	1,619.00	1764.00	−9.37	
G2-2	352.00	33.40	30.76	0.80	0.70	4.02	17.50	0.14	0.51	2,150.00	1730.00	−8.96	
L4	53.60	408.00	0.38	0.72	0.72	5.01	28.40	0.11	0.51	1,577.00	1749.00	−10.18	
	6.81	177.00	0.11	0.72	0.72	13.00	81.60	0.10	0.51	1,435.00	1732.00	−9.95	
	53.60	408.00	0.38	0.72	0.71	5.01	28.40	0.11	0.51	1,536.00	1704.00	−9.62	
Biotite granite	268.00	128.00	6.09	0.73	0.71	3.96	21.99	0.11	0.51	1,650.00	1790.00	−9.75	Zhao et al. (2015)
Biotite granite	261.00	149.00	5.09	0.73	0.71	4.36	26.09	0.10	0.51	1,540.00	1780.00	−9.59	
Biotite granite	229.00	144.00	4.60	0.73	0.71	4.38	25.51	0.10	0.51	1,590.00	1790.00	−9.75	
Biotite granite	266.00	133.00	5.81	0.73	0.71	4.73	27.99	0.10	0.51	1,580.00	1810.00	−9.95	
Biotite granite	272.00	138.00	5.70	0.73	0.72	3.80	20.63	0.11	0.51		1750.00	−9.10	Bai et al. (2014)
Biotite granite	269.00	91.50	8.53	0.74	0.71	4.20	24.67	0.10	0.51		1720.00	−8.74	
Biotite granite	271.00	123.00	6.37	0.74	0.72	5.07	28.72	0.11	0.51		1820.00	−9.95	

activity. The contemporaneous G1, G2-1, and G2-2 developed in the main body of the Guandimiao batholith. Lower Yanshanian igneous rocks (180–147 Ma) of the SCB, containing high K calc-alkaline I-type granitoids, are widespread and distributed as parallel belts. Upper Yanshanian igneous rocks contain early-stage granitic-volcanic rocks and late-stage mafic rocks in south-southeastern China. Correspondingly, the Yanshanian felsic and mafic dikes (G3 and L4) were emplaced at the center and margin of the Guandimiao batholith. Igneous rocks of the Guandimiao batholith contain a complete record of multiple stages of magmatism and tectonic events since the Indosinian.

6.2 Petrogenesis

6.2.1 Genesis type of granitic rocks

The S- and I-type scheme was initially proposed by Chappell and White (1974); Chappell and White (1992), and this letter scheme classification has been widely developed in later studies (Loiselle and Wones, 1979; Whalen et al., 1987; Eby, 1990; Eby, 1992; King et al., 1997; Bonin, 2007; etc.). The mineral assemblage, with the absence of typical alkaline mafic minerals, indicates I- and S-type granitic characteristics for Guandimiao granitoids. In addition, G1 and G2-1 of the Guandimiao batholith have low SiO2 and high FeOT contents and K/Na and FeO^T/MgO ratios; G2-2 and G3 are enriched in SiO$_2$ contents, Al$_2$O$_3$ contents, and K/Na ratios but depleted in MgO and CaO contents. The values of (Zr + Nb + Ce + Y) for the Guandimiao granitoids range from 138 to 295.7 ppm. The ΣREEs are 96.2–193 ppm, and 10,000 × Ga/Al ratios are 2.09–3.02.

These values are significantly lower than the lowest values observed in A-type granite (Whalen et al., 1987). Whole-rock Zr saturation temperatures suggest that crystallization temperatures (714–785°C) are consistent with crystallization temperatures < 800°C of I- and S-type granite rather than crystallization temperatures (>8 00°C, even possibly > 1,000°C) of A-type granite (Clemens et al., 1986). All samples plot in the S- and I-type granite fields on the FeO^T/MgO versus Zr + Nb + Ce + Y (Figure 9A).

On the ACF classification diagram, G2-2 and G3 plot in the S-type granite field, whereas G1 and G2-1 plot within the I-type granite field (Figure 9B).

6.2.2 Origin of the guandimiao batholith

The Pb isotope compositions of the Guandimiao granitoids present higher radiogenic Pb isotope compositions than syntectic granite and plot in the remelting granite of the South China field on the (^{207}Pb/^{204}Pb)$_i$ versus (^{208}Pb/^{204}Pb)$_i$ diagram and ^{207}Pb/^{204}Pb versus ^{206}Pb/^{204}Pb diagram. It is also above the mantle evolution line proposed by Hart (1984) (Figures 10A,B). This suggests that the Pb was mainly derived from the upper crust.

However, the existence of different genetic types (I- and S-type) and lithological compositions of intrusive rocks indicates diverse sources for the Guandimiao batholith (Chappell and White, 1974; Chappell et al., 1988). Zhou (2003) noted that the Indosinian granitoids are scattered across South China. Because of the uneven thickness of the Earth's crust, the granitoids are characterized by multiple sources and are dominated by thickened continental crust. G1 and G2-1 of the Guandimiao batholith enclosed mafic microgranular enclave,

TABLE 4 Pb isotopic compositions of igneous rocks in Guandimiao batholith.

Samples	U/ ppm	Th/ ppm	Pb/ ppm	^{206}Pb/^{204}Pb	^{207}Pb/^{204}Pb	^{208}Pb/^{204}Pb	^{206}Pb/^{207}Pb	μ	ω	Th/U	V1	Reference
HNGDM-2-1	6.37	28.00	44.70	239.00	18.71	15.71	39.11	9.65	38.64	3.88	91.25	This paper
HNGDM-2	9.66	24.30	24.20	153.00	19.21	15.74	39.08	9.66	36.16	3.62	97.02	
HNGDM-3	10.90	46.20	26.50	226.00	18.82	15.71	39.06	9.64	37.83	3.80	91.92	
HNGDM-4	6.83	50.10	31.40	226.00	18.61	15.71	38.98	9.65	38.62	3.87	84.59	
HNGDM-5-1	9.12	50.80	20.10	226.00	18.70	15.70	38.88	9.63	37.66	3.78	84.50	
HNGDM-6	6.29	16.40	32.70	18.95	15.71	39.87	1.21	9.63	40.30	4.05	107.46	
HNGDM-7	9.52	12.70	71.00	19.96	15.78	43.00	1.26	9.70	46.59	4.65	208.59	
HNGDM-8	6.35	13.70	34.80	19.48	15.77	40.91	1.24	9.70	41.80	4.17	146.06	
GDM11-4	6.34	26.10	38.39	223.00	18.63	15.76	39.29	9.75	40.24	3.99	92.41	Zhao et al. (2015)
GDM11-6	6.14	25.00	35.76	223.00	18.63	15.75	39.28	9.74	40.22	4.00	92.06	
GDM11-9	7.18	26.03	38.58	223.00	18.65	15.71	39.18	9.66	39.27	3.93	90.21	

Samples	V2	Δα	Δβ	Δγ	TSK/Ma	μ2	ω2	(Th/U)^2	(^{206}Pb/^{204}Pb)$_i$	(^{207}Pb/^{204}Pb)$_i$	(^{208}Pb/^{204}Pb)$_i$	Reference
HNGDM-2-1	67.68	96.51	25.55	54.27	168.00	10.09	40.93	3.93	18.36	15.69	38.61	This paper
HNGDM-2	88.98	118.96	26.98	49.68	−142.00	10.11	37.76	3.61	18.59	15.71	38.57	
HNGDM-3	73.28	102.14	25.62	52.26	89.00	10.07	39.83	3.83	17.88	15.66	37.75	
HNGDM-4	63.69	89.85	25.29	50.13	232.00	10.10	40.92	3.92	18.11	15.68	37.79	
HNGDM-5-1	69.10	95.12	24.90	47.44	154.00	10.05	39.58	3.81	17.66	15.65	36.99	
HNGDM-6	65.74	101.91	25.24	69.68	−7.00	10.05	42.94	4.14	18.31	15.68	39.79	
HNGDM-7	81.98	160.51	29.81	153.58	−604.00	10.19	51.09	4.85	19.72	15.77	42.94	
HNGDM-8	81.35	132.66	28.83	97.59	−279.00	10.19	45.12	4.29	18.97	15.74	40.83	
GDM11-4	62.18	90.81	28.41	58.37	312.00	10.31	43.48	4.08	18.20	15.73	38.72	Zhao et al. (2015)
GDM11-6	61.92	90.46	28.28	58.15	313.00	10.30	43.44	4.08	18.18	15.73	38.70	
GDM11-9	63.09	91.69	25.47	55.48	213.00	10.10	41.78	4.00	18.16	15.69	38.62	

TABLE 5 Formation ages of the ig rocks from Guandimiao batholith.

Sampling location	Lithology	Age/Ma	Method	Reference
Guandimiao	Two mica monzogranite	227.5 ± 1.0	LA	This paper
Guandimiao	Two mica monzogranite	225.5 ± 2.2	LA	
Guandimiao	Biotite monzogranite	226.2 ± 0.82	LA	
Guandimiao	Biotite monzogranite	225.9 ± 0.72	LA	
Guandimiao	Lamprophyre	121.22 ± 1.16	LA	
Guandimiao	Granite porphyry	189–211		
Guandimiao	Biotite granite	223.4 ± 1.7	LA	Zhao et al. (2015)
Guandimiao	Biotite granodiorite	239 ± 3	SHRIMP	Wang et al. (2005)
Guandimiao	Shizhuqiao two-mica alkali feldspar granite	226 ± 3	LA	Zhao et al. (2017)
Guandimiao	Jingtou hornblende-bearing biotite monzogranite	223 ± 2	LA	Zhao et al. (2017)
Guandimiao	Microgranular enclaves	220 ± 3	LA	Zhao et al. (2017)
Guandimiao	Granite	203–208		
Guandimiao	Granite	220 ± 3	LA	Miao B. F. (Unpublished),
Guandimiao	Monzonitic granite	230	K-Ar	Huang and Depaolo, (1989)
Zhoujialing	Biotite granite	203 ± 1.4	LA	Miao, (2014)
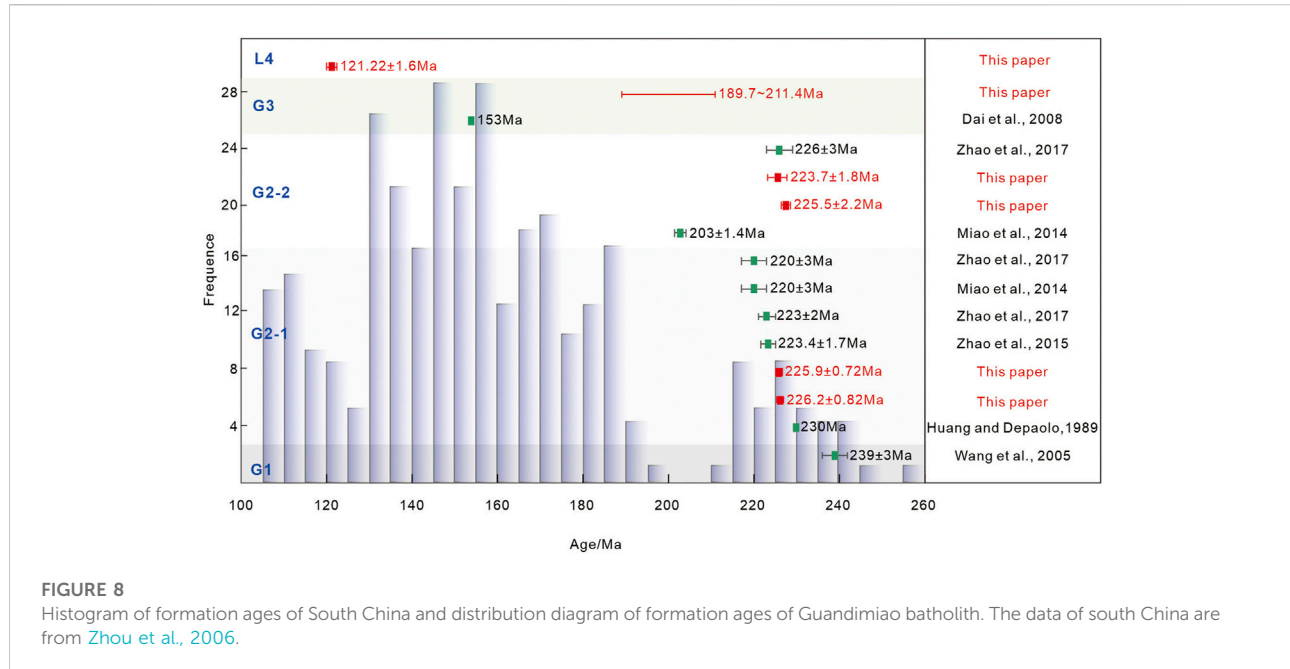
FIGURE 8
Histogram of formation ages of South China and distribution diagram of formation ages of Guandimiao batholith. The data of south China are from Zhou et al., 2006.
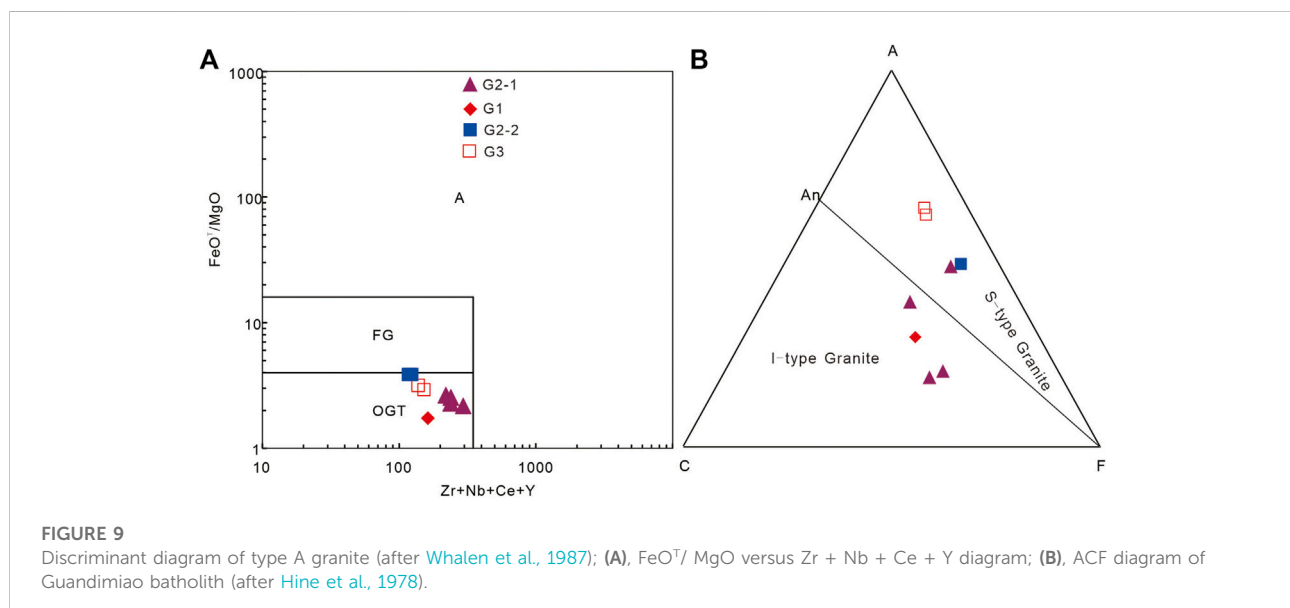
FIGURE 9
Discriminant diagram of type A granite (after Whalen et al., 1987); **(A)**, FeO^T/ MgO versus Zr + Nb + Ce + Y diagram; **(B)**, ACF diagram of Guandimiao batholith (after Hine et al., 1978).

which might have been formed by the rapid crystallization of mafic minerals upon chilling and reduction in viscosity instead of by the mixing of mantle-derived components (Vernon, 1984; Sparks and Marshall, 1986; Zhao et al., 2017).

In addition, G1 and G2-1 have obvious I-type granite affinities and are characterized by relatively high $\varepsilon N_d(t)$ values (−6.17 to −10.54), low initial $^{87}Sr/^{86}Sr$ ratios (0.712005–0.71758) and T_{DM2} values (1.52 Ga for G1 and 1.85 to 1.76 Ga for G2-1). G2-

2 and G3 show S-type granite affinities and have high initial $^{87}Sr/^{86}Sr$ ratios (0.7344) and T_{DM2} values (1.73 Ga for G2-2 and 1.93 Ga for G3) but lower $\varepsilon_{Nd}(t)$ values (−8.96 to −12.14). All samples show characteristics of crustal sources on the T versus $\varepsilon_{Nd}(t)$ diagram (Figure 11A). The AMF [molar $Al_2O_3/(FeO^T + MgO)$] values of G1 and G2-1 range from 1.36 to 1.65, much lower than the values of G2-2 and G3 (3.59–4.63). The CMF [molar $CaO/(FeO^T + MgO)$] values of G1 and G2-1 are between 0.47 and 0.62, whereas the G2-2
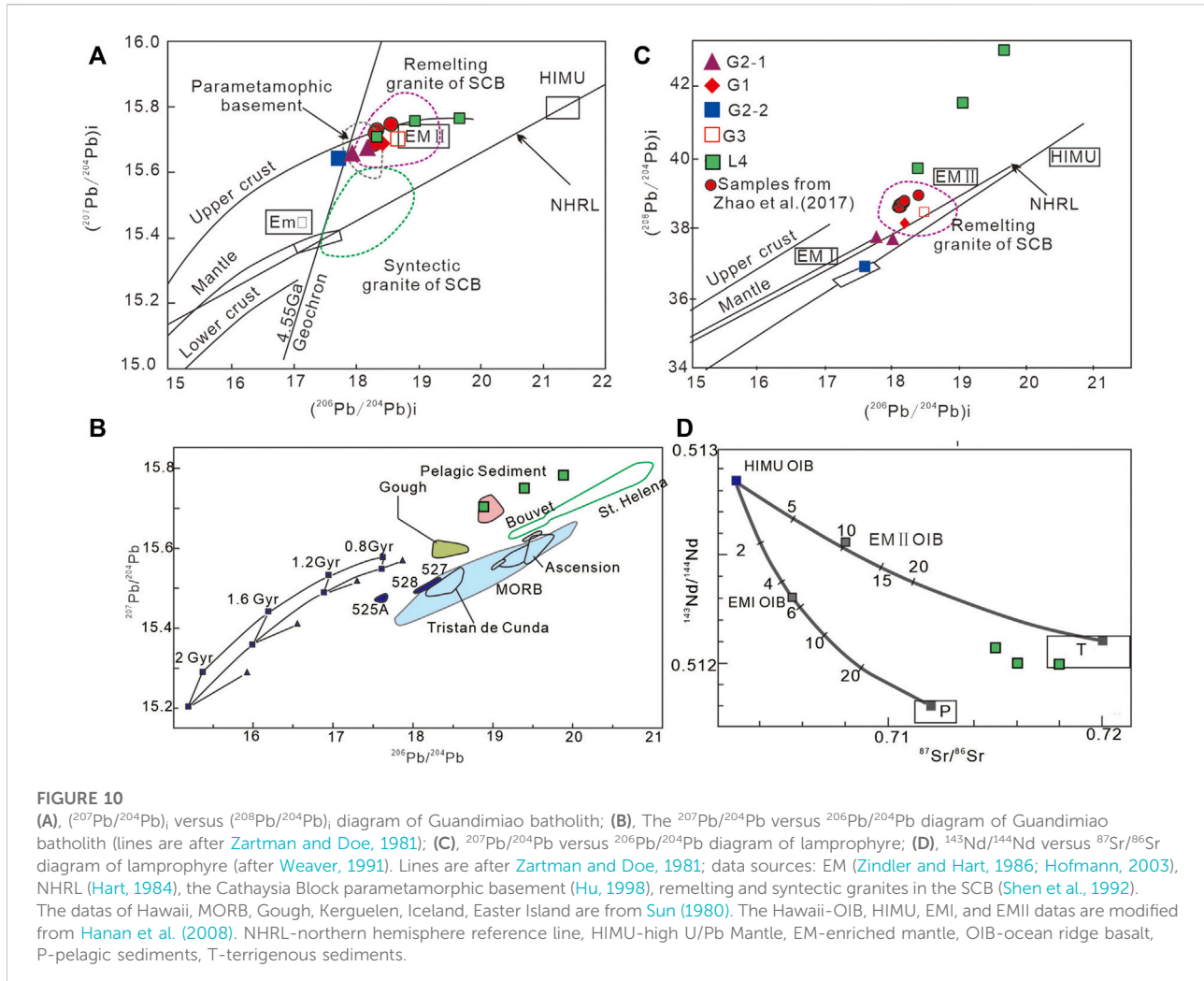
FIGURE 10
(A), $(^{207}Pb/^{204}Pb)_i$ versus $(^{208}Pb/^{204}Pb)_i$ diagram of Guandimiao batholith; **(B)**, The $^{207}Pb/^{204}Pb$ versus $^{206}Pb/^{204}Pb$ diagram of Guandimiao batholith (lines are after Zartman and Doe, 1981); **(C)**, $^{207}Pb/^{204}Pb$ versus $^{206}Pb/^{204}Pb$ diagram of lamprophyre; **(D)**, $^{143}Nd/^{144}Nd$ versus $^{87}Sr/^{86}Sr$ diagram of lamprophyre (after Weaver, 1991). Lines are after Zartman and Doe, 1981; data sources: EM (Zindler and Hart, 1986; Hofmann, 2003), NHRL (Hart, 1984), the Cathaysia Block parametamorphic basement (Hu, 1998), remelting and syntectic granites in the SCB (Shen et al., 1992). The datas of Hawaii, MORB, Gough, Kerguelen, Iceland, Easter Island are from Sun (1980). The Hawaii-OIB, HIMU, EMI, and EMII datas are modified from Hanan et al. (2008). NHRL–northern hemisphere reference line, HIMU–high U/Pb Mantle, EM–enriched mantle, OIB–ocean ridge basalt, P–pelagic sediments, T–terrigenous sediments.

and G3 values range from 0.24 to 0.27. On the diagram of AFM versus CFM, G1 and G2-1 are derived from metabasaltic to metatonalitic source fields, which is consistent with the Jingtou granite, which was derived from a high-K calc-alkaline amphibolite source with metabasaltic to metatonalitic compositions (Figure 11B; Altherr et al., 2000; Zhao et al., 2017). In contrast, G2-2 and G3 plot near the Shizhuqiao granite field, indicating a source similar to the para-metamorphic basement of the Cathaysia Block (Shen et al., 1993; Altherr et al., 2000; Zhao et al., 2015; Zhao et al., 2017).

Moreover, the variation features of two stages of Sm-Nd isotope model ages show an inhomogeneous source. The T_{DM2} of G1 is much younger than those of metamorphosed basement in the Cathaysia block (1.8–2.2 Ga) and might be derived from the remelting of meta-juvenile crust in the Mesoproterozoic. The T_{DM2} values of G2-1, G2-2 and *G3* range from 1.74 to 1.93 Ga, which is consistent with the Paleoproterozoic metamorphosed basement of the Cathaysia block. These results amply justify their geological affiliation. L4 of the Guandimiao batholith has low $\varepsilon_{Nd}(t)$ values (−10.18 to −9.62) but high I_{sr} (0.71449–0.71784)

and T_{DM2} values (1.75–1.70 Ga), which represents significant deviation from the Mesozoic EM II-type OIB in the SCB (6.8–10.8; Meng et al., 2012; Qin et al., 2020). The $^{207}Pb/^{204}Pb$ versus $^{207}Pb/^{204}Pb$ and $^{143}Nd/^{144}Nd$ versus $^{87}Sr/^{86}Sr$ diagrams show that L4 was derived from a Mesoproterozoic pelagic and/or terrigenous sediment source (Figures 10C,D).

Garnet and spinel were mainly La-, Sm-, and Yb-bearing minerals in the magma source. They are significantly insensitive and can be used as an indicator to trace the melt source and the degree of partial melting (Aldanmaz et al., 2000; Zhao and Zhou, 2008). As the partial melting of a garnet lherzolite occurred in the source, the Sm/Yb ratio decreased sharply, while the La/Sm ratio decreased gradually. The partial melting of garnet lherzolite produces higher Sm/Yb ratios than spinel lherzolite melting (Johnson, 1994; Aldanmaz et al., 2000). The La/Sm versus Sm/Yb and Sm/Yb versus Yb diagrams show that the lamprophyre samples plot near the garnet lherzolite melting curves. These results suggest that the lamprophyre was mainly formed by partial melting of garnet lherzolite. However, a wide
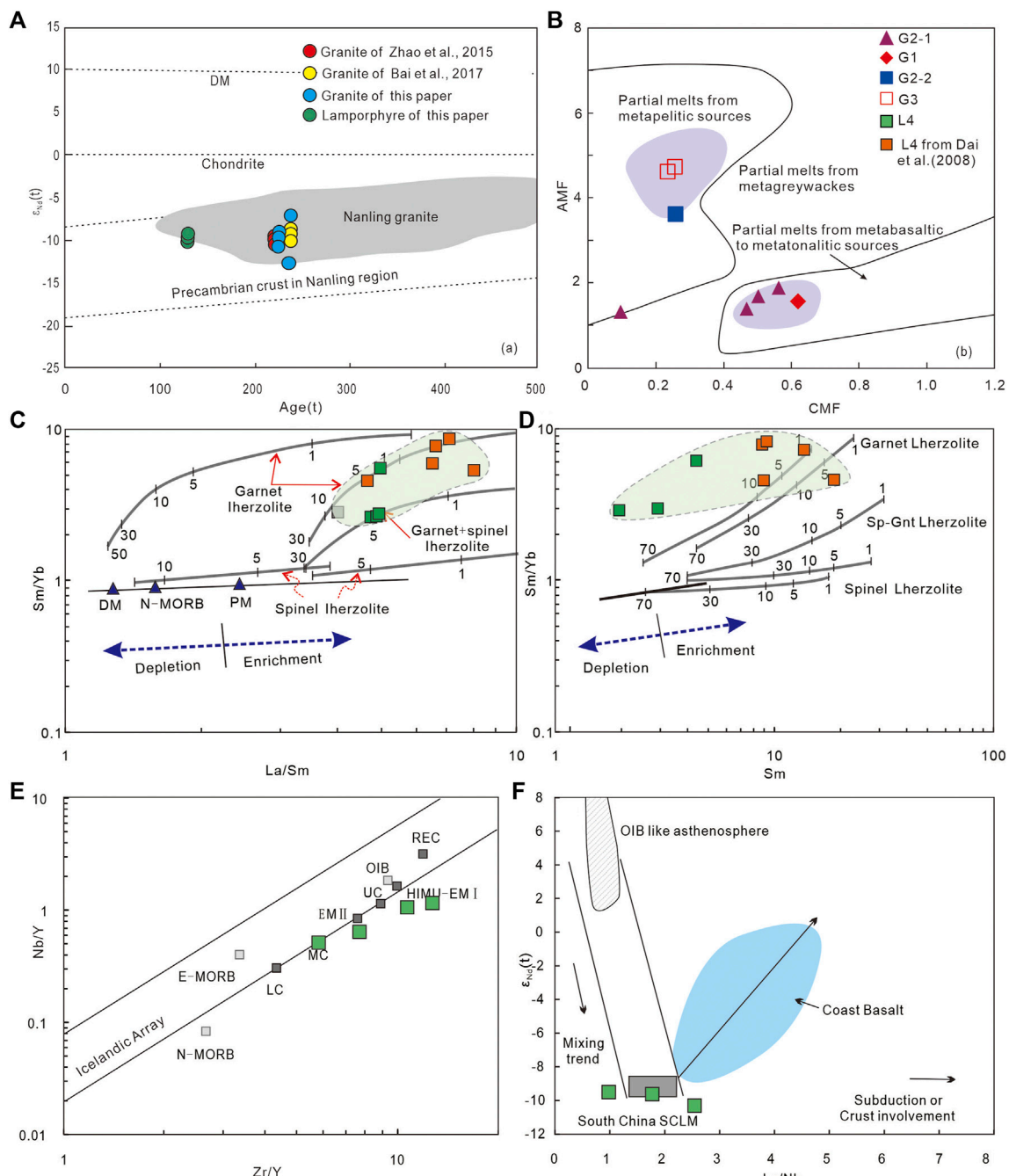
FIGURE 11
(A), ε_{Nd} (t) versus Age diagram; (B), AMF versus CMF diagram; (C,D), Sm/Yb versus La/Yb diagram and Sm/Yb versus Sm of lamprophyre; (E), Nb/Y versus Zr/Y diagram; (F), ε_{Nd} (t) versus La/Nb diagrams. Data source: Nanling granite (Yuan and Zhang, 1992), Precambrian crust in Nanling region (Shen et al., 1993). The gray field data from Zhao et al., 2015; Zhao et al., 2017; Orange samples from Dai et al., 2008; Coast Basalt field from Meng et al. (2012); South China SCLM from Chen et al. (2008b). Panels (C,D) are modified after Aldanmaz et al. (2000); DM from Mckenzie and Keith, 1995, N-MORB and PM from Sun and McDonough (1989). Melting curves of Spinel lherzolite (Ol53 + Opx 27 + Cpx 17 + Sp 11) and Garnet lherzolite (Ol 60 + Opx 20 + Cpx 10 + Gt 10) are from Aldanmaz et al. (2000).

degree of partial melting is also presented in Figures 11C,D, which indicates extensive crustal contamination. The same conclusion can also be drawn from the Nb/Y versus Zr/Y and

ε_{Nd}(t) versus La/Nb diagrams. The lamprophyre samples deviate from the Iceland array and plot in the field of mixing trends between the OIB-like asthenosphere and South China SCLM. It
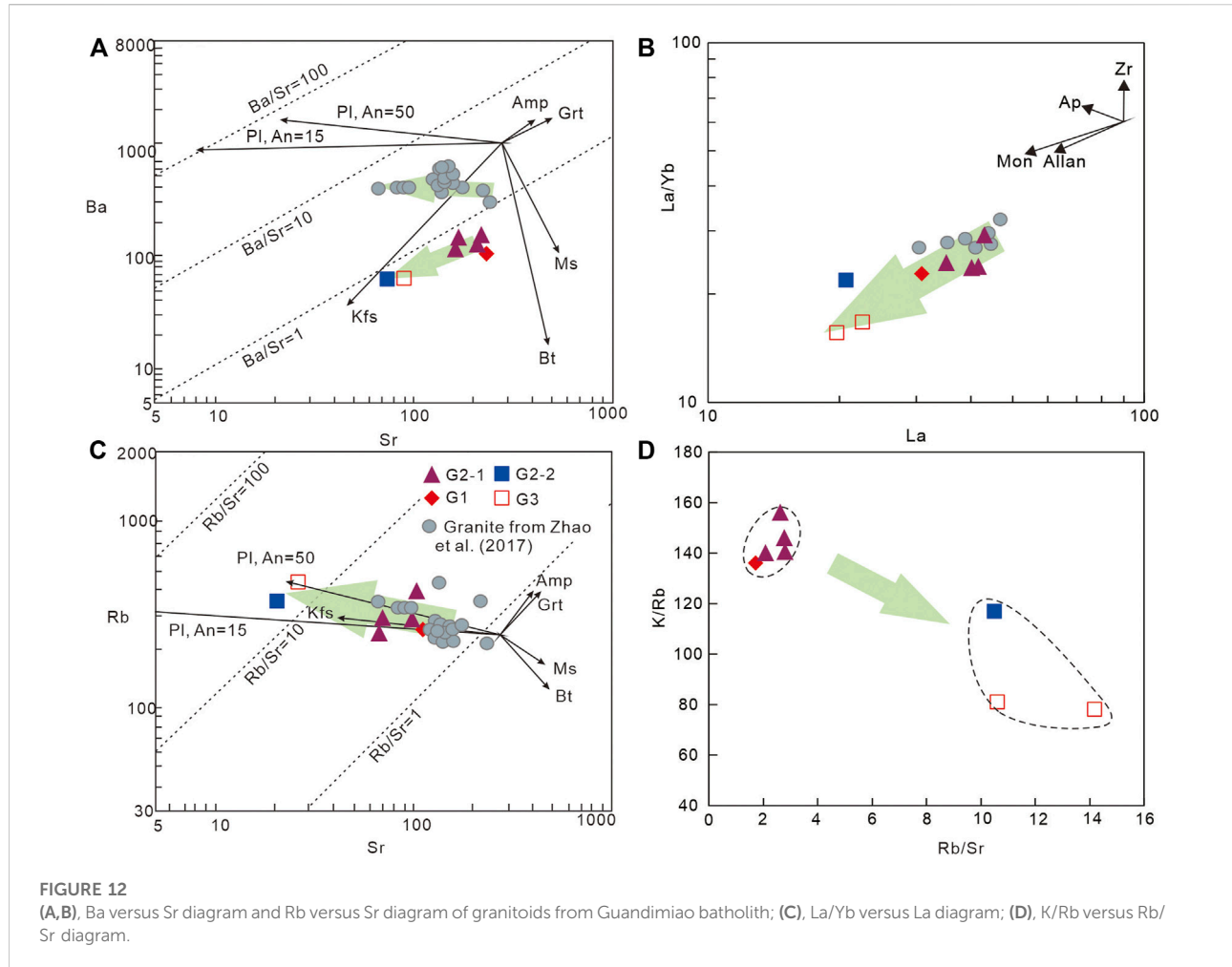
FIGURE 12
(A,B), Ba versus Sr diagram and Rb versus Sr diagram of granitoids from Guandimiao batholith; **(C)**, La/Yb versus La diagram; **(D)**, K/Rb versus Rb/Sr diagram.

shows strong crustal information (Condie, 2005; Meng et al., 2012; Figures 15E,F).

6.2.3 Magmatism

During granitic magmatism, the main Ti-bearing minerals (ilmenite, rutile, titanite, anatase, etc.) could lead to a significant depletion of Ti, Nb, Ta, etc. The fractional crystallization of apatite could significantly decrease the P concentration in the residual melt. Eu, Sr, and Ba could be depleted during fractional crystallization of feldspar, as they usually substitute K^+ and Ca^{2+} sites into K-feldspar and/or plagioclase. In the Guandimiao batholith, there is significant depletion in Ba, Nb, Sr, and Ti for G2-2 and G3 but less depletion in Ba, Nb, Sr, P, and Ti for G1 and G2-1. This may suggest that the Guandimiao granitoids experienced obvious fractional crystallization of feldspar, Ti-bearing minerals and apatite at the early stages of magmatism. In addition, the negative correlations between Ba and Sr and between Rb and Sr suggest that the magmatic system underwent intense fractional crystallization of K-feldspar and plagioclase (Figures 12A,B). For the rare earth elements (La and Yb), carrier

minerals include zircon, apatite, allanite, monazite, etc. The negative relationship between La and La/Yb suggests that the fractional crystallization of allanite and monazite also played an important role in the evolution of magmatism (Figure 12C). It is worth mentioning that G1 and G2-1 have higher K/Rb ratios and lower Rb/Sr ratios than G2-2 and G3. More proof is required that the late stage of magmatism was higher in the degree of fractionation than the early stage (Figure 12D). The granitoids of the Guandimiao batholith were the result of multistage differentiation of an identical long-term magma chamber.

6.3 Implications for tectonic evolution

6.3.1 Complete record of the pre-mesozoic tectonic event of the SCB

Nine stages of lamprophyre (*L4*) fully reveal the episodic growth of the South China plate (Figure 13B). Similar evidence has been reported by Shu (2012) and Shu et al. (2020). Five time
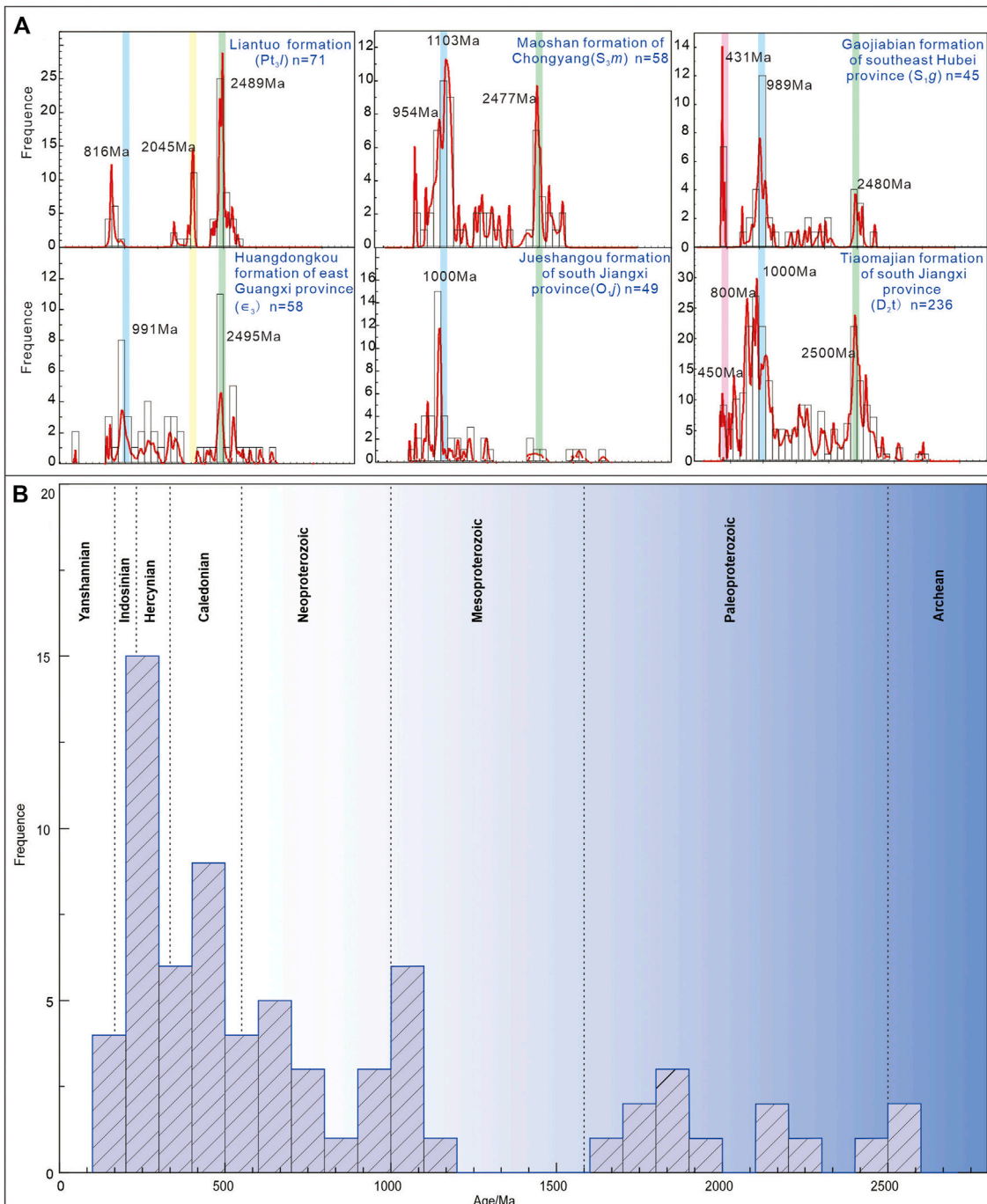
FIGURE 13
(A), Histogram of model ages of detrital zircons of South China, **(B)**, histogram of zircon U–Pb ages of lamprophyre from Guandimiao batholith.

intervals of detrital zircons dating from the Jinggangshan–Nanling region (2.56–2.38 Ga; 1.93–1.52 Ga; 1.3–0.9 Ga; 0.85–0.73 Ga; and 0.68–0.55 Ga) have been identified. The 5 time intervals could also be identified by detrital zircons from Hubei Province (Gaojiabei Formation),

Jiangxi (Huangdongkou Formation, Jueshangou Formation and Tiaomajian Formation), Guangdong Province (gneiss), Sichuan Province (Pingyipu Formation), and Guizhou Province (Dazhuyuan Formation; Shu, 2012; Zhao et al., 2013; Wang D. H. et al., 2014; Wang X. L. et al., 2014) (Figure 13A).
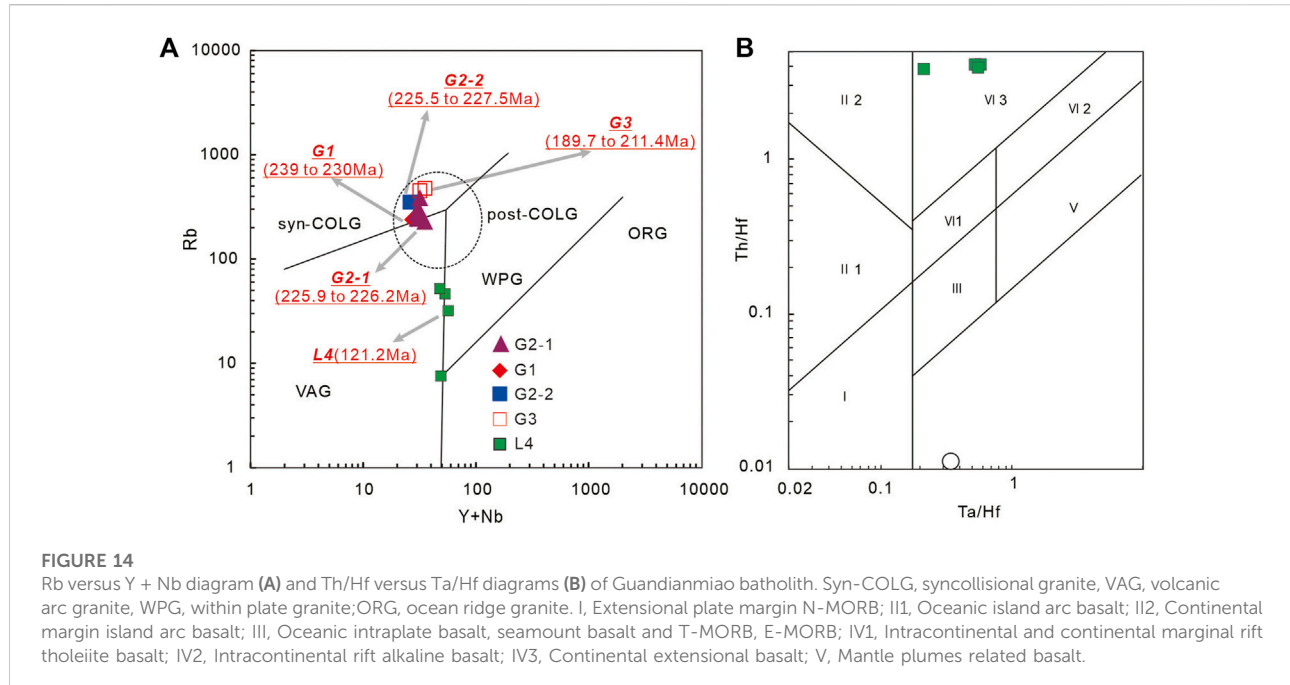
FIGURE 14
Rb versus Y + Nb diagram **(A)** and Th/Hf versus Ta/Hf diagrams **(B)** of Guandianmiao batholith. Syn-COLG, syncollisional granite, VAG, volcanic arc granite, WPG, within plate granite;ORG, ocean ridge granite. I, Extensional plate margin N-MORB; II1, Oceanic island arc basalt; II2, Continental margin island arc basalt; III, Oceanic intraplate basalt, seamount basalt and T-MORB, E-MORB; IV1, Intracontinental and continental marginal rift tholeiite basalt; IV2, Intracontinental rift alkaline basalt; IV3, Continental extensional basalt; V, Mantle plumes related basalt.

The Neoarchean to Paleoproterozoic ages (2,573.1–2,447.3 Ma) were extensively derived from xenolith crystals in mafic dikes and clastic zircons in Paleozoic strata (Zheng et al., 2008). They are obviously younger than the Kongling Group in the Yangtze block (3.3 Ga, Ma et al., 1997). They represent global continental nucleus growth events and mixing processes between Neoarchean mafic magma and more ancient crustal components.

The middle to late Paleoproterozoic data (2,232.7–2,114.4 Ma and 1931.6–1,625.9 Ma) is linked to the response of the convergence and breakup effect of the Columbia supercontinent. The convergence of the Columbia supercontinent began 2.1 Ga, which is represented by the formation of the Kora-Kareline conjunctive craton and West Australian craton and the outgrowth of the western Amazon ancient continental plate margin in South America (Hoffman, 1988). Correspondingly, significant tectonic magmatic events were also recorded in the North China craton (NCC) and Yangtze craton (Zhang et al., 2006; Yin et al., 2013). Subsequently, the tectonic regime transformed to breakup on a global scale 1.7–1.5 Ga. A large number of A-type granitoids and mafic dikes developed in the Yangtze craton, indicating the existence of intracontinental rifting (Rogers and Santosh, 2002; Zhao et al., 2002; Evans and Mitchell, 2011; Gibson et al., 2012; Geng et al., 2019).

During the early Neoproterozoic (1,135.0–769.7 Ma), the region experienced the suture of the Paleo-Huanan Ocean along the Jiangnan–Shaoxing large fault zone, and the collision between the Yangtze block and Cathaysia block created the initial appearance of the ancient SCB. This was completely documented by abundant ophiolites and associated pyroclastic rocks developed along the

Dexin–Dongxiang and Zhuji–Lishui–Wuyi–Meixi belts in the southeastern Cathaysia block from 1.0–0.9 Ga. The I-type granite and mafic rocks of the southern Jiangnan orogenic belt, which formed 0.9–0.8 Ga, indicates the subduction of pristine oceanic crust (Ye et al., 2007; Shu et al., 2012; Zhou et al., 2018). The subsequent break-up of the supercontinent and extension events occurred along the paleo-suture and formed the Nanhua continental rift basin and three main tectonic domains (Nanling, Wuyi, and Yunkai) 825–760 Ma (Wang et al., 2017; Yang et al., 2018). The eventual Phanerozoic collage of the SCB (early Paleozoic, 466.8–405.3 Ma) and multistage intracontinental orogenic events (late Paleozoic, 268.0–258.8 Ma; 379.6–295.9 Ma) constituted the basic tectonic appearance in the Paleozoic (Liu et al., 1990; Shu et al., 2006; Shu et al., 2012).

6.3.2 Mesozoic tectonic evolution of the SCB

The Guandimiao batholith is the central part of the SCB. The G1, G2-1 and G2-2 phases were emplaced 239–203 Ma and were dominant in the period from 230 to 220 Ma. The structural discriminant diagram shows that these rocks formed in a postcollisional environment (Figure 14A; post-COLG field; Pearce, 1996). The lamprophyre plots near the WPG field and VI₃ field on the Rb versus Y + Nb diagram (intraplate basalt) (Figure 14B), which indicates an intracontinental extensional setting.

During the early Indosinian (250–240 Ma), the forceful collision and extensive metamorphism between the Indo-China block and the Sibumas-Qingtang block occurred in the Early-Middle Triassic and exerted a profound impact on the
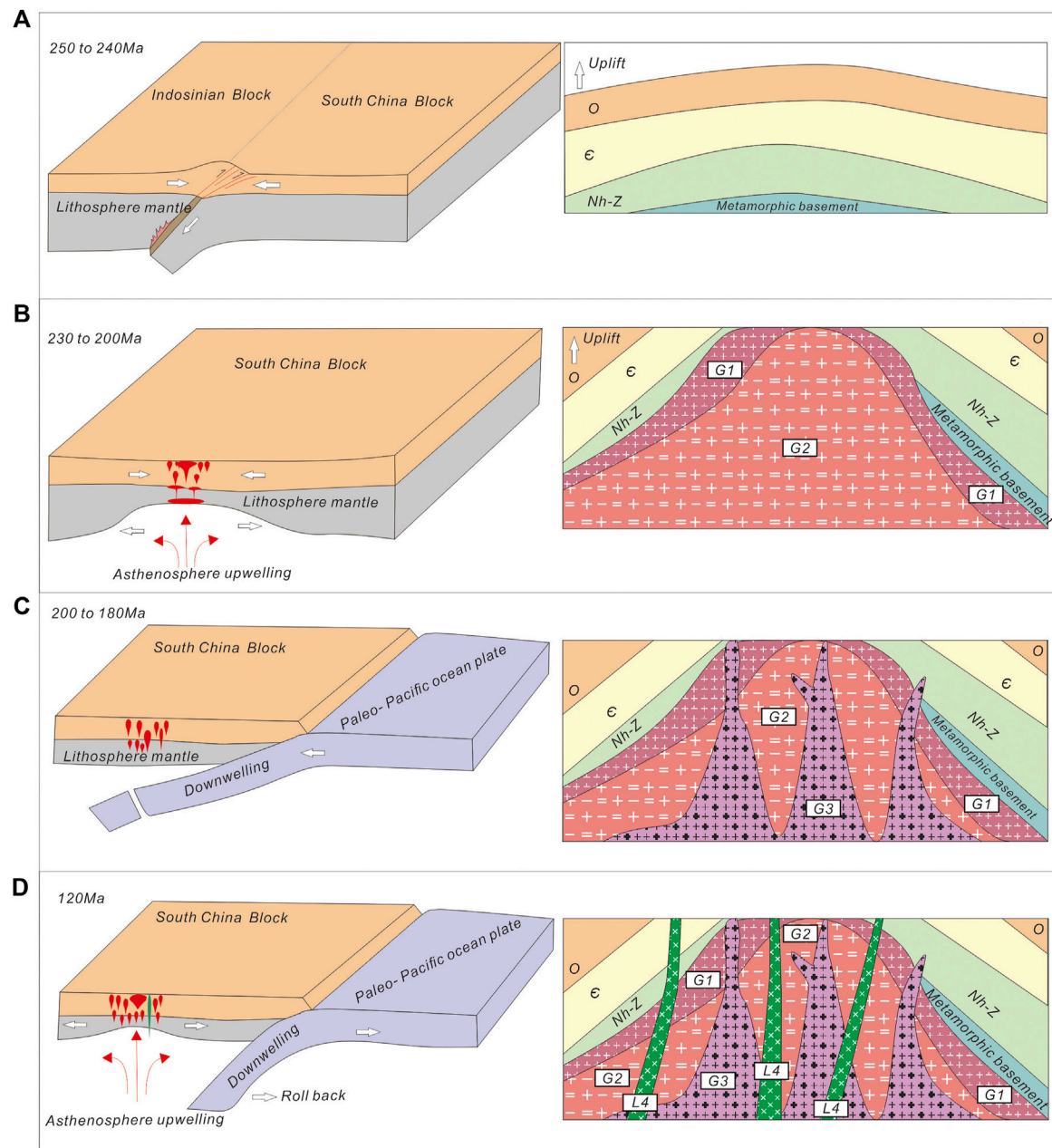
FIGURE 15
The brief model diagram of the tectonic evolution of south China at Mesozoic and the emplacement model of Guandimiao batholith. **(A)** the early Indosinian period (250–240 Ma); **(B)** the late Indosinian period (230–220 Ma); **(C)** the early Yanshanian period (200–180 Ma); **(D)** the late Yanshanian period (120 Ma).

southeastern Eurasian continent (Chen et al., 2002; Li et al., 2006). Meanwhile, the closure of the Paleo-Tethys Ocean caused southeastward subduction and collision between the NCC and the SCB. The SCB underwent multidirectional compression and massive shortening, accompanied by an approximately 50 km thickening of the continental lithosphere (Tapponnier et al., 1982; Gilder et al., 1995; Carter et al., 2001; Wang et al., 2002; Li et al., 2017) (Figure 15A). The collisional orogenic events

immensely shortened the crust and resulted in a series of thrust faults and uplift structures. There was an approximately 10 Myr. Interval before granitoids melted following the end of crustal thickening (Patio Dounce et al., 1990), and Sylvester (1998) proposed a possible relaxation and thinning of the thickened crust with a time interval of 10–20 Myr. The Guandimiao dome developed at the center of the SCB. The main part of the Guandimiao batholith was formed in a postcollision setting

after the Indosinian crustal thickening events in the SCB. The thermal stress from crustal extension caused decompression and melting of thickened crust, along with continuous emplacement of mantle-derived magma (Pape et al., 2012). It induced extensive melting of Paleoproterozoic metamorphic basement in the SCB (Zhou et al., 2006; Guo et al., 2012; Qin et al., 2022) (Figure 15B).

Approximately 200–180 Ma, the transformation of the tectonic regime occurred from NE-directed paleo-Tethys ocean dominance to NE-directed paleo-Pacific ocean dominance. The continued subduction of the paleo-Pacific plate beneath the Eurasian plate affected more than 1,000 kilometers. Due to the stable structure and the shortage of transcrustal faults, there was a significant deficiency in magmatic rocks, and the volume and scale of magmatism were far less than those developed either in the early Insinian or late Mesozoic and have been confirmed as the break-in period (200–180 Ma) of igneous rocks in South China (Mao et al., 2004; Zhang et al., 2009) (Figure 15C). Scattershot intrusions occurred as stocks and dikes exposed in the interior batholith with limited scope.

In the Middle Jurassic, subduction of the paleo-Pacific oceanic plate converted to rollback steep subduction and caused large-scale extensional events in the back-arc basin. The uplift of asthenospheric mantle melted the ancient metamorphic basement and formed a large granitic melt 135–118 Ma (Zhou et al., 2006; Jiang et al., 2015; Yang, 2018; Li et al., 2019). Moreover, mafic magma rapidly intruded along the deeply penetrating faults and extensively contaminated the upper crustal materials. This made it possible for the formation of lamprophyre with intense crustal information (L4) (Figure 15D).

7 Conclusion

1 The Guandimiao batholith was dominated by four stages of magmatism. The granodiorite formed at 239 Ma (Stage 1). The biotite monzogranite (G2-1) and two-mica monzogranite (G2-2) formed at 230–203 Ma (Stage 2). The granite porphyry formed from 211 to 190 Ma (Stage 3). The lamprophyre (L4) formed 121 Ma (Stage 4).

2 G1 and G2-1 have I-type granite affinity, while G2-2 and G3 show S-type granite characteristics. G1 was derived from the remelting of meta-juvenile crust in the Mesoproterozoic. G2-1, G-2, and G3 were derived from the Paleoproterozoic metamorphosed basement of the Cathaysia block. The source of L4 was garnet and spinel lherzolite, which underwent mixing between the Mesoproterozoic pelagic and/or terrigenous sediment and SCLM of South China. The granitoids of the Guandimiao batholith underwent intensely fractional crystallization of feldspar, Ti-bearing minerals, allanite and monazite.

3 The zircon U-Pb dating of L4 in the Guandimiao batholith completely records the six stages of pre-Mesozoic tectonic events in the SCB. During the Mesozoic, the main body of the Guandimiao batholith (G1, G2-1, and G2-2) recorded the closure of the paleo-Tethys Ocean in the Triassic and the subsequent regional extension of the postcollision. The dikes of the Guandimiao batholith documented the transition of tectonic and dynamic regimes in the early Yanshanian and the rollback and steep subduction of the paleo-Pacific Ocean in the late Yanshanian.

Data availability statement

The original contributions presented in the study are included in the article/Supplementary Material, further inquiries can be directed to the corresponding author.

Author contributions

Conceptualization, J-HQ and FH; methodology, J-HQ; software, J-HQ; validation, FH and D-HW; formal analysis, J-HQ; investigation, J-HQ and FH; resources, J-HQ; data curation, D-HW; writing—original draft preparation, J-HQ; writing—review and editing, J-HQ and FH; visualization, J-HQ; supervision, D-HW; project administration, D-HW; funding acquisition, D-HW. All authors have read and agreed to the published version of the manuscript.

Funding

Conflict of interest

The authors declare that the research was conducted in the absence of any commercial or financial relationships that could be construed as a potential conflict of interest.

Publisher's note

All claims expressed in this article are solely those of the authors and do not necessarily represent those of their affiliated organizations, or those of the publisher, the editors and the reviewers. Any product that may be evaluated in this article, or claim that may be made by its manufacturer, is not guaranteed or endorsed by the publisher.

References

Aldanmaz, E., Pearce, J. A., Thirlwall, M. F., and Mitchell, J. G. (2000). Petrogenetic evolution of late cenozoic, post-collision volcanism in Western anatolia, Turkey. *J. Volcanol. Geotherm. Res.* 102 (1-2), 67–95. doi:10.1016/S0377-0273(00)00182-7

Altherr, R., Holl, A., Hegner, E., Langer, C., and Kreuzer, H. (2000). High-potassium, calc-alkaline I-type plutonism in the European Variscides, northern Vosges (France) and northern Schwarzwald (Germany). *Lithos* 50 (1), 51–73. doi:10.1016/s0024-4937(99)00052-3

Bai, D. Y., Zhong, X., Jia, P. Y., Xiong, X., and Huang, W. Y. (2014). Geochemistry and petrogenesis of the Indosinian Guandimiao granitic pluton in central Hunan. *Sediment. Geol. Tethyan Geol.* 34 (4), 93–105. (in Chinese with English abstract).

Barbarin, B. (2005). Mafic magmatic enclaves and mafic rocks associated with some granitoids of the central sierra Nevada batholith, California: Nature, origin, and relations with the hosts. *Lithos* 80 (1-4), 155–177. doi:10.1016/j.lithos.2004.05.010

Bonin, B. (2007). A-Type granites and related rocks: Evolution of a concept, problems and prospects. *Lithos* 97, 1–29. doi:10.1016/j.lithos.2006.12.007

Carter, A., Roques, D., Bristow, C., and Kinny, P. (2001). Understanding mesozoic accretion in southeast Asia, significance of triassic thermotectonism. *Geology* 29 (29), 211–214. doi:10.1130/0091-7613(2001)029<0211:UMAISA>2.0.CO;2

Chappell, B. W., White, A. J. R., and Hine, R. (1988). Granite provinces and basement terranes in the lachlan fold belt, southeastern Australia. *Aust. J. Earth Sci.* 35 (4), 505–521. doi:10.1080/08120098808729466

Chappell, B. W., and White, A. J. R. (1992). I- and s-type granites in the lachlan fold belt. *Earth Environ. Sci. Trans. R. Soc. Edinb.* 83 (1-2), 1–26. doi:10.1017/S0263593300007720

Chappell, B. W., and White, A. J. R. (1974). Two contrasting granite types, Pacific. *Geology* 8, 173–174. doi:10.1046/j.1440-0952.2001.00882.x

Chen, C. H., Lee, C. Y., Lu, H. Y., and Hsieh, P. S. (2008b). Generation of Late Cretaceous silicic rocks in SE China, age, major element and numerical simulation constraints. *J. Asian Earth Sci.* 31, 479–498. doi:10.1016/j.jseaes.2007.08.002

Chen, C. H., Lee, C. Y., and Shinjo, R. (2008a). Was there jurassic paleo-pacificsubduction in south China? Constraints from $^{40}Ar/^{39}Ar$ dating, elemental and Sr–Nd–Pb isotopic geochemistry of the mesozoic basalt. *Lithos* 106, 83–92. doi:10.1016/j.lithos.2008.06.009

Chen, P., Hua, R., Zhang, B., Lu, J., and Fan, C. (2002). Early Yanshanian post-orogenic granitoids in the Nanling region. *Sci. China Ser. D-Earth. Sci.* 45 (8), 755–768. doi:10.1007/bf02878432

Chen, Y. C., Wang, D. H., Xu, Z. G., and Huang, F. (2014). Outline of regional metallogeny of ore deposits associated with the Mesozoic magmatism in South China. *Geotect. Metallogenia* 38 (2), 219–229. (in Chinese with English abstract). doi:10.3969/j.issn.1001-1552.2014.02.002

Cheng, Y. Q. (1994). *Concise regional geology of China*. Beijing: Geological Publishing House, 1–539. (in Chinese).

Clemens, J. D., Holloway, J. R., and White, A. J. R. (1986). Origin of A type granites: Experimental constraints. *Am. Mineral.* 71, 317–324. (in Chinese with English abstract).

Condie, K. C. (2005). High field strength element ratios in Archean basalt, a window to evolving sources of mantle plumes? *Lithos* 79 (3-4), 491–504. doi:10.1016/j.lithos.2004.09.014

Dai, F. Y., Chen, B. H., and Liu, F. G. (2008). Characteristics and geological significance of vein rocks in guandimiao area, hunan province. *Land Resour. Her.* 5 (1), 33–36. (in Chinese with English abstract). doi:10.3969/j.issn.1672-5603.2008.01.013

Deng, J., Wang, C. M., Zi, J. W., Xia, R., and Li, Q. (2017). Constraining subduction-collision processes of the paleo-tethys along the changning-menglian suture: New zircon U-Pb ages and Sr-Nd-Pb-Hf-O isotopes of the Lincang batholith. *Gondwana Res.* 62, 75–92. doi:10.1016/j.gr.2017.10.008

Deng, P., Ren, J. S., Ling, H. F., Sun, L. Q., Zhu, B., and Tan, Z. Z. (2012). SHRIMP zircon U-Pb ages and tectonic implications for Indosinian granitoids of southern Zhuguangshan granitic composite, South China. *Chin. Sci. Bull.* 57 (14), 1542–1552. doi:10.1007/s11434-011-4951-8

Depaolo, D. J. (1981). Trace element and isotopic effects of combined wallrock assimilation and fractional crystallization. *Earth Planet. Sci. Lett.* 53 (2), 189–202. doi:10.1016/0012-821x(81)90153-9

Eby, G. N. (1992). Chemical subdivision of the A-type granitoids, Petrogenetic and tectonic implications. *Geol.* 20, 641. doi:10.1130/0091-7613(1992)020<0641:csotat>2.3.co;2

Eby, G. N. (1990). The A-type granitoids: A review of their occurrence and chemical characteristics and speculations on their petrogenesis. *Lithos* 26, 115–134. doi:10.1016/0024-4937(90)90043-z

Evans, D. A. D., and Mitchell, R. N. (2011). Assembly and breakup of the core of Paleoproterozoic-mesoproterozoic supercontinent Nuna. *Geology* 39 (5), 443–446. doi:10.1130/G31654.1

Geng, Y. S., Kuang, H. W., Du, L. L., Liu, Y. Q., and Zhao, T. P. (2019). On the Paleo-Mesoproterozoic boundary from the breakup event of the Columbia supercontinent. *Acta Petrol. Sin.* 35 (8), 2299–2324. (in Chinese with English abstract). doi:10.18654/1000-0569/2019.08.02.10.18654/1000-0569/2019.08.02

Gibson, G. M., Henson, P. A., Neumann, N. L., Southgate, P. N., and Hutton, L. J. (2012). Paleoproterozoic-earliest Mesoproterozoic basin evolution in the Mount Isa region, northern Australia and implications for reconstructions of the Nuna and Rodinia supercontinents. *Episodes* 35 (1), 131–141. doi:10.18814/epiiugs/2012/v35i1/012

Gilder, S. A., Coe, R. S., Wu, H., Kuang, G., Zhao, X., Qi, W., et al. (1995). Triassic paleomagnetic data from south China and their bearing on the tectonic evolution of the Western circum-pacific region. *Earth Planet. Sci. Lett.* 131 (3), 269–287. doi:10.1016/0012-821x(95)00030-g

Gilder, S. A., and Courtillot, V. (1997). Timing of the north-south China collision from new middle to late mesozoic paleomagnetic data from the north China block. *J. Geophys. Res.* 102 (B8), 17713–17727. doi:10.1029/97JB01201

Gilder, S. A., Gill, J., Coe, R. S., Zhao, X. X., Liu, Z. W., and Wang, G. X. (1996). Isotopic and paleomagnetic constraints on the Mesozoic tectonic evolution of south China. *J. Geophys. Res.* 101 (B7), 16137–16154. doi:10.1029/96JB00662

Greentree, M. R., Li, Z. X., Li, X. H., and Wu, H. (2006). Late mesoproterozoic to earliest neoproterozoic basin record of the sibao orogenesis in Western south China and relationship to the assembly of rodinia. *Precambrian Res.* 151 (1), 79–100. doi:10.1016/j.precamres.2006.08.002

Guo, C. L., Zheng, J. H., Lou, F. S., and Zeng, Z. L. (2012). Petrography, genetic types and geological dynamical setting of the Indosinian granitoids in South China. *Geol. Metallogenia* 36 (3), 457–472. (In Chinese with English abstract). doi:10.1007/s11783-011-0280-z

Hanan, B. B., Shervais, W. J., and Vetter, S. (2008). Yellowstone plume-continental lithosphere interaction beneath the snake river plain. *Geol.* 36 (1), 51–54. doi:10.1130/G23935A.1

Hart, S. R. (1984). A large-scale isotope anomaly in the southern hemisphere mantle. *Nature* 309 (5971), 753–757. doi:10.1038/309753a0

Hervé, F., Pankhurst, R. J., and Yaxley, G. (2007). the South patagonian batholith: 150 my of granite magmatism on a plate margin. *Lithos* 97 (3-4), 373–394. doi:10.1016/j.lithos.2007.01.007

Hine, R., Williams, I. S., Chappell, B. W., and White, A. J. R. (1978). Contrasts between I- and S-type granitoids of the kosciusko batholith. *J. Geol. Soc. Aust.* 25 (3-4), 219–234. doi:10.1080/00167617808729029

Hofmann, A.W. (2003). Sampling mantle heterogeneity through oceanic basalts: Isotopes and trace elements. *Treatise on Geochem.* 2, 1–44. doi:10.1016/B0-08-043751-6/02123-X

Hoffman, P. F. (2003). Continental transform tectonics: Great Slave Lake shear zone (ca. 1.9 Ga), northwest Canada. *Geology* 15, 7852–7889. doi:10.1130/0091-7613

Hu, G. R. (1998). *Study on Geological Geochemistry, Isotopic chronogy and metamorphic P-T-t path of metamorphic rock belt in ccentral Jiangxi*. China: Nanjing University. (in Chinese with English abstract).

Huang, X., and Depaolo, D. J. (1989). Study of sources of paleozoic granitoids and the basement of south China by mean of Nd-Sr isotope. *Acta Petrol. Sin.* 5 (1), 28–36. (in Chinese with English abstract).

Jiang, Y. H., Wang, G. C., Zheng, L., Ni, C. Y., Qing, L., Zhang, Q., et al. (2015). Repeated slab advance-retreat of the Palaeo-Pacific plate underneath SE China. *Int. Geol. Rev.* 57 (4), 472–491. doi:10.1080/00206814.2015.1017775

Johnson, K. T. M. (1994). Experimental cpx/ and garnet/ melt partitioning of REE and other trace elements at high pressures; petrogenetic implications. *Mineral. Mag.* 58, 454–455. doi:10.1180/minmag.1994.58A.1.236

King, P. L., White, A. J. R., Chappell, B. W., and Allen, C. M. (1997). Characterization and origin of aluminous A-type granites from the Lachlan Fold Belt, southeastern Australia. *J. Petrology* 38, 371–391. doi:10.1093/petroj/38.3.371

Li, S. Z., Jahn, B. M., Zhao, S. J., Da, L. M., Li, X. Y., Suo, Y. H., et al. (2017). Triassic southeastward subduction of north China block to south China block:

Insights from new geological, geophysical and geochemical data. *Earth-Science Rev.* 166, 270–285. doi:10.1016/j.earscirev.2017.01.009

Li, X. H., Li, Z. X., Ge, W., Zhou, H., and Wingate, M. T. D. (2003). Neoproterozoic granitoids in South China: Crustal melting above a mantle plume at ca. 825 Ma? *Precambrian Res.* 122 (1), 45–83. doi:10.1016/s0301-9268(02)00207-3

Li, X. H., Li, Z. X., and Li, W. X. (2014). Detrital zircon U-Pb age and Hf isotope constrains on the generation and reworking of precambrian continental crust in the Cathaysia block, south China: A synthesis. *Gondwana Res.* 25 (3), 1202–1215. doi:10.1016/j.gr.2014.01.003

Li, X. H., Li, Z. X., Li, W. X., and Wang, Y. J. (2006). Initiation of the indosinian orogeny in south China: Evidence for a permian magmatic arc on hainan island. *J. Geol.* 114, 341–353. doi:10.1086/501222

Li, X. H., Li, Z. X., Li, W. X., Ying, L., Yuan, C., and Wei, G. (2007). U-Pb zircon, geochemical and Sr-Nd-Hf isotopic constraints on age and origin of jurassic I- and A-type granites from central guangdong, SE China: A major igneous event in response to foundering of a subducted flat-slab? *Lithos* 96 (1-2), 186–204. doi:10. 1016/j.lithos.2006.09.018

Li, X. H., Li, Z. X., Zhou, H. W., Liu, Y., and Kinny, P. D. (2002). U-Pb zircon geochronology, geochemistry and Nd isotopic study of Neoproterozoic bimodal volcanic rocks in the Kangdian rift of South China, implications for the initial rifting of Rodinia. *Precambrian Res.* 113 (1), 135–154. doi:10. 1016/s0301-9268(01)00207-8

Li, X. H. (1990). Magmatic age and crustal movement of the wanyangshan-Zhuguangshan granite complex batholith. *Sci. China* 7, 747–755. (In Chinese).

Li, X. H., Zhou, H. W., and Liu, Y. (2001). Mesozoic shoshonitic intrusives in the Yangchun basin, Western guangdong, and their tectonic significance, ii. trace elements and Sr-Nd isotopes. *Geochimica* 30, 57–65. (in Chinese with English abstract). doi:10.3321/j.issn:0379-1726.2001.01.007

Li, Z. X., and Li, X. H. (2007). formation of the 1300 km-wide intra-continental orogen and postorogenic magmatic province in mesozoic south China: A flat-slab subduction model. *Geol.* 35, 179. doi:10.1130/G23193A.1

Li, Z. X., Li, X. H., Kinny, P. D., and Wang, J. (1999). The breakup of Rodinia; did it start with a mantle plume beneath south China? *Earth Planet. Sci. Lett.* 173 (3), 171–181. doi:10.1016/S0012-821X(99)00240-X

Liang, X. Q., and Guo, D. L. (2002). Deep tectonic activation and its shellow response in Hunan province. *Chin. J. Geol.* 3, 332–342. (in Chinese with English abstract). doi:10.3321/j.issn:0379-1726.2001.01.007

Liu, B. J. (1994). *Lithofacies paleogeographic atlas of south China*. Beijing: Science Press, 1–239. (in Chinese with English abstract).

Liu, B. J., Zhou, M. K., and Wang, R. Z. (1990). Early palaeozoic palaeogeography and tectonic evolution of south China. *Acta Geosci. Sin.* 1, 97–98. (In Chinese with English abstract).

Loiselle, M. C., and Wones, D. R. (1979). Characteristics and origin of anorogenic granites. *Geol. Soc. Am. Prog. Abstr.* 12 (7), 468.

Ludwig, K. R. (2003). *Isoplot/ex, a geochronological toolkit for microsoft excel, version 3.00*. United States: Berkeley Geochronology Center.

Ma, D. H., Li, Z. C., and Xiao, Z. F. (1997). A Study on the boundary age between Jurassic and Cretaceous. *Acta Geoscientia Sinica* 3, 233–241. (in Chinese with English abstract).

Ma, X. X., Dong, C. W., Tang, L. M., Lv, Q., and Gu, H. Y. (2013). Petrological evidence of mesozoic tectonic extension in the coastal area of SE China, the spatial-temporal distribution and geochemical constraints on the mafic rocks from Hainan, Guangdong, Fujian and Zhejiang Provinces, South China. *J. Zhejiang Univ. Sci. Ed.* 40 (6), 683–692. doi:10.3785/j.issn.1008-9497.2013.06.015

Mao, J. R., Li, Z. L., and Ye, H. M. (2014). Mesozoic tectono-magmatic activities in South China: Retrospect and prospect. *Sci. China Earth Sci.* 44 (12), 2853–2877. doi:10.1007/s11430-014-5006-1

Mao, J. W., Chen, C. H., Yuan, S. D., and Guo, C. L. (2011). Characteristics and spatial-temporal regularity of mineral deposits in qinhang (or shihang) metallogenic belt, south China. *Acta Geol. Sin.* 85 (5), 636–658. (in Chinese with English abstract).

Mao, J. W., Xie, G. Q., Li, X. F., Zhang, C. Q., and Mei, Y. X. (2004). Meosozoic large scale mineralization and multiple lithospheric extension in South China. *Earth Sci. Front.* 11 (1), 45–55. China University of Geosciences, Beijing (in Chinese with English abstract). doi:10.3321/j.issn:1005-2321.2004.01.003

Mao, J. W., Xie, G. Q., Li, X. F., Zhang, Z. H., Wang, Y. T., and Wang, Z. L. (2005). Geodynamic process and metallogeny, history and present research trend, with a special discussion on continental accretion and related metallogeny throughout geological history in South China. *Mineral. Deposits* 24 (3), 193–205. (in Chinese with English abstract). doi:10.3969/j. issn.0258-7106.2005.03.001

Mckenzie, D., and Keith, O. R. (1995). The Source Regions of Ocean Island Basalts. *J. Petrol.* 1, 133–159. doi:10.1093/petrology/36.1.133

Meng, L. F., Li, Z. X., Chen, H., Li, X. H., and Wang, X. C. (2012). Geochronological and geochemical results from mesozoic basalts in southern south China block support the flat-slab subduction model. *Lithos* 132 (132-133), 127–140. doi:10.1016/j.lithos.2011.11.022

Miao, B. H. (2014). *Geologic characteristic and genesis mechanism of the qingshuitang Pb-Zn deposit in Qidong county, hunan province*. China: Nanjing University, 1–80. (in Chinese with English abstract).

Nasdala, L., Hofmeister, W., Norberg, N., Martinson, J. M., Corfu, F., Dörr, W., et al. (2008). Zircon M257–A homogeneous natural reference material for the ion microprobe U-Pb analysis of Zircon. *Geostand. Geoanal. Res.* 32 (3), 247–265. doi:10.1111/j.1751-908X.2008.00914.x

Pape, F. L., Jones, A. G., Vozar, J., and Wei, W. (2012). Penetration of crustal melt beyond the kunlun fault into northern tibet. *Nat. Geosci.* 5 (5), 330–335. doi:10. 1038/NGEO1449

Patio Dounce, A. E., Humphreys, E. D., and Johnston, A. D. (1990). Anatexis and metamorphism in tectonically thickened continental crust exemplified by the Sevier hinterland, Western North America. *Earth Planet. Sci. Lett.* 97, 290–315. doi:10. 1016/0012-821X(90)90048-3

Pearce, J. (1996). Sources and settings of granitic rocks. *Episodes* 19 (4), 120–125. doi:10.1002/(SICI)1096-9837(199612)21:12<1163::AID-ESP666>3.3.CO

Qin, J. H., Wang, D. H., and Chen, Y. C. (2022). Geochemical and geochronological constraints on a granitoid containing the largest indosinian tungsten (W) deposit in south China (SC): Petrogenesis and implications. *Minerals* 12 (1), 80. doi:10.3390/min12010080

Qin, J. H., Wang, D. H., and Chen, Y. C. (2020). Geochemical and Sr-Nd-Pb isotopic characteristics of basalt from eastern Hunan Province: New insight for the Late Cretaceous tectonic dynamic mechanism in South China. *Geol. J.* 55 (12), 8141–8168. doi:10.1002/gj.3914

Rogers, J. J. W., and Santosh, M. (2002). Configuration of Columbia, a mesoproterozoic super-continent. *Gondwana Res.* 5 (1), 5–22. doi:10.1016/ S1342-937X(05)70883-2

Rowley, D. B., Jiayu, R., Jin, Z., Yuan-Dong, Z., and Ren-Bing, Z. (1997). Late precambrian through early paleozoic stratigraphic and tectonic evolution of the nanling region, Hunan Province, south China. *Int. Geol. Rev.* 39 (5), 469–478. doi:10.1080/00206819709465285

Rubatto, D. (2002). Zircon trace element geochemistry, Partitioning with garnet and the link between U-Pb ages and metamorphism. *Chem. Geol.* 84, 123–138. doi:10.1016/S0009-2541(01)00355-2

Shen, W. Z., Chen, F. R., Liu, C. S., and Wang, D. Z. (1992). Isotopic-geochemical characteristics and source material for two types of volcanic-intrusive complexes in Jiangxi Province. *Acta Petrol. Sin.* 8 (2), 177–184. (in Chinese with English abstract).

Shen, W. Z., Zhu, J. C., Liu, C. S., Xu, S. J., and Ling, H. F. (1993). Sm-Nd isotopic study of basement metamorphic rocks in south China and its constraint on material sources of granitoids. *Acta Petrol. Sin.* 9, 115–124. (in Chinese with English abstract).

Shu, L. S. (2012). An analysis of principal features of tectonic evolution in South China Block. *Geol. Bull. China* 31 (7), 1035–1053. (in Chinese with English abstract). doi:10.1111/j.1755-6724.2008.tb00581.x

Shu, L. S., Chen, X. Y., and Lou, F. S. (2019). Pre-jurassic tectonics of the south China. *Acta Geol. Sin.* 94 (2), 333–360. doi:10.1111/j.1755-6724.2008. tb00581.x

Shu, L. S., Zhou, X. M., Deng, P., and Yu, X. Q. (2006). Principal geological features of nanling tectonic belt, south China. *Geol. Rev.* 52 (2), 251–265. (in Chinese with English abstract). doi:10.3969/j.issn.1671-2552.2006.03.002

Shu, L. S., and Zhou, X. M. (2002). Late mesozoic tectonism of southeast China. *Geol. Rev.* 48 (3), 249–260. (in Chinese with English abstract). doi:10.3321/j.issn: 0371-5736.2002.03.004

Shu, L. S. (2012). An analysis of pricipal features of tectonic evolution in South China Block. *Geol. Bullet. China* 31 (7), 1035–1053. (in Chinese with English abstract). doi:10.3969/j.issn.1671-2552.2012.07.003

Shu, L. S., Chen, X. Y., and Lou, F. S. (2020). Pre-Jurassic tectonics of the SouthChian. *Acta Geologica Sinica* 94 (2), 333–360.

Sláma, J., Košler, J., Condon, D. J., Crowley, J. L., Gerdes, A., Hanchar, J. M., et al. (2008). Plešovice zircon-a new natural reference material for U-Pb and Hf isotopic microanalysis. *Chem. Geol.* 249, 1–35. doi:10.1016/j.chemgeo.2007. 11.005

Sparks, R. S. J., and Marshall, L. A. (1986). Thermal and mechanical constraints on mixing between mafic and silicic magmas. *J. Volcanol. Geotherm. Res.* 29 (1), 99–124. doi:10.1016/0377-0273(86)90041-7

Sun, S. S. (1980). Lead isotopic study of young volcanic rocks from midocean ridges, ocean islands and island arcs, Philos. *Trans. R. Soc. Lond.* 297, 409–445. doi:10.1098/rsta.1980.0224

Sun, S. S., and McDonough, W. F. (1989). *Chemical and systematics of oceanic basalts, Implication for mantle 682 composition and processes*, 42. London: Geological Society of London. Special Publication, 313–345. doi:10.1144/GSL.SP.1989.042.01.19

Sun, T. (2006). A new map showing the distribution of granites in South China and its egplauatory notes. *Geol. Bull. China* 25 (3), 332–337. (in Chinese with English abstract). doi:10.3969/j.issn.1671-2552.2006.03.002

Sylvester, P. J. (1998). Post-collisional strongly peraluminous granites. *Lithos* 45, 29–44. doi:10.1016/S0024-4937(98)00024-3

Tapponnier, P., Peltzer, G., Le Dain, A. Y., Armijo, R., and Cobbold, P. (1982). Propagating extrusion tectonics in Asia, new insights from simple experiments with plasticine. *Geol.* 10 (12), 611. doi:10.1130/0091-7613(1982)10<611:petian>2.0.co;2;2

Vernon, R. H. (1984). Microgranitoid enclaves in granites-globules of hybrid magma quenched in a plutonic environment. *Nature* 309 (5967), 438–439. doi:10.1038/309438a0

Wang, Y. J., Fan, W. M., Liang, X. Q., Peng, T. P., and Shi, Y. R. (2005). Zircon SHRIMP U-Pb age and genetic revelation of Indosinian granites in Hunan. *Chinese Science Bulletin* 50 (12), 1259–1266. (in Chinese with English abstract). doi:10.3321/j.issn:0023-074X.2005.12.018

Wang, D. H., Chen, Z. H., Chen, Y. C., Tang, J. X., Li, J. K., Ying, L. J., et al. (2010). New data of the rock forming and ore-forming chronology for China's important mineral resources areas. *Acta Geol. Sin.* 84 (7), 1030–1040. (in Chinese with English abstract).

Wang, D. H., Chen, Z. Y., Huang, F., Wang, C. H., Zhao, Z., Chen, Z. H., et al. (2014). Discussion on metallogenic specialization of the magmatic rocks and related issues in the Nanling Region. *Geotect. Metallogenia* 38 (2), 230–238. (in Chinese with English abstract).

Wang, X. L., Zhou, J. C., GriIIin, W. I., Zhao, G. C., Yu, J. H., Qiu, J. S., et al. (2014). Geochemical zonation across a Neoproterozoic orogenic belt isotopic evidence from granitoids and metasedimentary rocks of the Jiangnan orogen, China. *Precambrian Res.* 242, 154–171. doi:10.1016/j.precamres.2013.12.023

Wang, D. H., Li, P. G., Qu, W. J., Lei, Z. Y, Liao, Y. C., et al. (2013). Discovery and preliminary study of the high tungsten and lithium contents in the Dazhuyuan bauxite deposit, Guizhou, China. *Sci. China Earth Sci.* 56, 145–152. doi:10.1007/s11430-012-4504-2

Wang, X. L., Zhou, J. C., C'hen, X., Zhang, F. F., and Sun, Z. M. (2017). Formation and evolution of the jiangnan orogen. *Bull. Mineralogy, Petrology Geochem.* 360, 714–735. (in Chinese with English abstract). doi:10.3969/j.issn.1007-2802.2017.05.003

Wang, Y., Guan, T. Y., Liu, P. H., Yu, D. J., and Wu, J. H. (2002). Nd and Sr isopotic geochemical characteristics for Early Cretaceous volcanic rocks in Northeast Jiangxi Province. *J. Mineralogy Petrology* 22 (1), 36–40. (in Chinese with English abstract). doi:10.1080/12265080208422884

Wang, Y. J., Fan, W. M., Cawood, P. A., and Li, S. Z. (2008). Sr–Nd–Pb isotopic constraints on multiple mantle domains for Mesozoic mafic rocks beneath the South China Block hinterland. *Lithos* 106, 297–308. doi:10.1016/j.lithos.2008.07.019

Wang, Y. J., Fan, W. M., Guo, F., Peng, T. P., and Li, C. W. (2003). Geochemistry of Mesozoic mafic rocks adjacent to the Chenzhou-Linwu Fault, South China, implications for the lithospheric boundary between the Yangtze and Cathaysia blocks. *Int. Geol. Rev.* 45, 263–286. doi:10.2747/0020-6814.45.3.263

Wang, Y. J., Fan, W. M., Liang, X. Q., Peng, T. P., and Shi, Y. R. (2005a). Zircon SHRIMP U-Pb age and genetic revelation of Indosinian granites in Hunan. *Chin. Sci. Bull.* 50 (12), 1259–1266. (in Chinese with English abstract). doi:10.3321/j.issn:0023-074X.2005.12.018

Wang, Y. J., Fan, W. M., Peng, T. P., and Guo, F. (2005b). Elemental and Sr-Nd isotopic systematics of the early mesozoic volcanic sequence in southern jiangxi province, south China, petrogenesis and tectonic implications. *Int. J. Earth Sci.* 94 (1), 53–65. doi:10.1007/s00531-004-0441-4

Weaver, B. L. (1991). The origin of ocean Island basalt end-member compositions, trace element and isotopic constraints. *Earth Planet. Sci. Lett.* 104 (2-4), 381–397. doi:10.1016/0012-821X(91)90217-6

Whalen, J. B., Kenneth, L. C., and Bruce W. C. (1987). A-type granites, geochemical characteristics, discrimination and petrogenesis. *Contrib. Mineral. Pet..* 95, 407–419. doi:10.1007/bf00402202

Whalen, J. B., Wodicka, N., Taylor, B. E., and Jackson, G. D. (2010). Cumberland batholith, trans-hudson orogen, Canada: Petrogenesis and implications for paleoproterozoic crustal and orogenic processes. *Lithos* 117 (1-4), 99–118. doi:10.1016/j.lithos.2010.02.008

Wu, Y. B., and Zhen, Y. F. (2004). Study on zirconium gallstone by mineralogy and its restriction on U-Pb age explanation. *Chin. Sci. Bull.* 49, 1589–1604. (in Chinese with English abstract).

Xia, W. C. (1991). Genetic stratigraphic framwork and its genetic relationship to oil and gas in Mesozoic and Cenozoic fault-controlled basin of Eastern China. *Geol. Sci. Technol. Inf.* 10 (1), 43–50. (in Chinese with English abstract).

Yang, F., Santosh, M., and Kim, S. W. (2018). Mesozoic magmatism in the eastern North China Craton: Insights on tectonic cycles associated with progressive craton destruction. *Gondwana Res.* 60, 153–178. doi:10.1016/j.gr.2018.04.003

Yang, F., Santosh, M., Kim, S. W., Zhou, H., and Jeong, Y. J. (2020). Late mesozoic intraplate rhyolitic volcanism in the north China craton: Far-field effect of the westward subduction of the paleo-Pacific plate. *GSA Bull.* 132 (1-2), 291–309. doi:10.1130/B35123.1

Yang, F., Xue, F., Santosh, M., Wang, G., Kim, S. W., Shen, Z., et al. (2019). Late mesozoic magmatism in the east qinling orogen, China and its tectonic implications. *Geosci. Front.* 10 (5), 1803–1821. doi:10.1016/j.gsf.2019.03.003

Yang, Z. (2012). *Pre-yanshanian magmatism and its mineralization in the miaoershan-yuechengling area, northern guangxi province.* China: Nanjing University, 1–64. (in Chinese with English abstract).

Yang, F., Santosh, M., and Kim, S. W. (2018). Mesozoic magmatism in the eastern North China Craton: Insights on tectonic cycles associated with progressive craton destruction. *Gondwana Research* 60, 153–178. doi:10.1016/j.gr.2018.04.003

Ye, M. F., Li, X. H., Li, W. X., Liu, Y., and Li, Z. X. (2007). SHRIMP zircon U-Pb geochronological and whole-rock geochemical evidence for an early Neoproterozoic Sibaoan magmatic arc along the southeastern margin of the Yangtze Block. *Gondwana Res.* 12 (1–2), 144–156. doi:10.1016/j.gr.2006.09.001

Yin, C. Q., Lin, S. F., Davis, D. W., Zhao, G. C., Xiao, W. J., Li, L. M., et al. (2013). 2.1–1.85Ga tectonic events in the Yangtze Block, South China: Petrological and geochronological evidence from the Kongling Complex and implications for the reconstruction of supercontinent Columbia. *Lithos* 183, 200–210. doi:10.1016/j.lithos.2013.10.012

Yuan, Z. X., and Zhang, Z. Q. (1992). Sm-Nd isotopic of granitoids in the nanling region and their petro-genetic analysis. *Geol. Rev.* 38 (1), 1–15. doi:10.16509/j.georeview.1992.01.001

Zartman, R. Z., and Doe, B. R. (1981). Plumbotectonics-themodel. *Tectonophysics* 75, 135–162. doi:10.1016/0040-1951(81)90213-4

Zhang, H. F., Sun, M., Zhou, X. H., Fan, W. M., Zhai, M. G., Yin, J. F., et al. (2002). Mesozoic lithosphere destruction beneath the north China craton, evidence from major-trace-element and Sr-Nd-Pb isotope studies of fangcheng basalts. *Contrib. Mineral. Pet..* 144 (2), 241–254. doi:10.1007/s00410-002-0395-0

Zhang, L., Chen, Z. Y., Wang, F. Y., and Zhou, T. F. (2020). Apatite geochemistry as an indicator of petrogenesis and uranium fertility of granites: A case study from the zhuguangshan batholith, south China. *Ore Geol. Rev.* 128, 103886. doi:10.1016/j.oregeorev.2020.103886

Zhang, Y. X. (1984). Ring structiure and their genetic mechanism in the South China region. *Geol. Rev.* 30 (5), 437–445. (in Chinese with English abstract).

Zhang, S. B., Zheng, Y. F., Wu, Y. B., Zhao, Z. F., Gao, S., and Wu, F. Y. (2006). Zircon isotope evidence for ≥3.5Ga continental crust in the Yangtze craton of China. *Precambrian Research* 146 (1–2), 16–34. doi:10.1016/j.precamres.2006.01.002

Zhang, S. H., Zheng, Y. F., He, Z. F., and Wu, H. (2009). The 1.35Ga diabase sills from the northern North China Craton: Implications for breakup of the Columbia (Nuna) supercontinent. *Earth and Planetary Science Letters* 288 (3-4), 588–600. doi:10.1016/j.epsl.2009.10.023

Zhao, J. H., and Zhou, M. F. (2008). Neoproterozoic adakitic plutons in the northern margin of the Yangtze block, China, partial melting of a thickened lower crust and implications for secular crustal evolution. *Lithos* 104 (1-4), 231–248. doi:10.1016/j.lithos.2007.12.009

Zhao, K. D., Jiang, S. Y., Yang, S. Y., Dai, B. Z., and Lu, J. J. (2012). Mineral chemistry, trace elements and Sr–Nd–Hf isotope geochemistry and petrogenesis of Cailing and Furong granites and mafic enclaves from the Qitianling batholith in the Shi-Hang zone, South China. *Gondwana Res.* 22 (1), 310–324. doi:10.1016/j.gr.2011.09.010

Zhao, T. P., Zhou, M, F., Zhai, M. G., and Xia, B. (2002). Paleoproterozoic rift-related volcanism of the xiong'er group, north China craton: Implications for the breakup of Columbia. *Int. Geol. Rev.* 44 (4), 336–351. doi:10.2747/0020-6814.44.4.336

Zhao, Z. H., Bao, Z. H., and Zhang, B. Y. (1998). Geochemistry of the mesozoic basaltic rocks in southern Hunan province. *Sci. China Ser. D-Earth. Sci.* 41 (1), 102–112. doi:10.1007/BF02875640

Zhao, Z., Miao, B., Xu, Z., Lu, J., Lei, L., Zuo, C., et al. (2017). Petrogenesis of two types of late triassic granite from the guandimiao complex, southern hunan province, China. *Lithos* 282-283, 403–419. doi:10.1016/j.lithos.2017.02.021

Zhao, Z., Wang, D. H., Li, P. G., and Lei, Z. Y. (2013). Detrital zircon U-Pb geochronology of the Dazhuyuan formation in Northern Uuizhou; implications for bauxite mineralization. *Rock Mineral analysis* 32 (1), 166–173. (in Chinese with English abstract). doi:10.3969/j.issn.0254-5357.2013.01.027

Zhao, Z. X., Xu, Z. W., Miao, B. H., Zuo, C. H., Lu, J. J., Lu, R., et al. (2015). Diagenetic age and material source of the guandimiao granitic batholith, hengyang city, hunan province. *Acta Geol. Sin.* 89 (7), 1219–1230. (in Chinese with English abstract). doi:10.3969/j.issn.0001-5717.2015.07.006

Zheng, J. P., Griffin, W. L., Tang, H. Y., Zhang, Z. H., Su, Y. P., and Liu, G. P. (2008). Archean basement similar to the north China and Yangtze continents may Be existed beneath the western Cathaysia. *Geol. J. China Univ.* 4, 549–557. (in Chinese with English abstract). doi:10.3969/j.issn.1006-7493.2008.04.008

Zhong, Y. F., Ma, C. Q., Yu, Z. B., Lin, G. C., Xu, H. J., Wang, R. J., et al. (2005). SHRIMP U-Pb zircon geochronology of the jiuling granitic complex batholith in jiangxi province. *Earth Science-Journal China Univ. Geosciences* 30 (6), 685–681. (in Chinese with English abstract). doi:10.3321/j.issn:1000-2383.2005.06.005

Zhou, J. L., Li, X. H., Tang, U. Q., Uao, B. Y., Bao, Z. A., Ling, X. X., et al. (2018). Ca. 890 Ma magmatism in the northwest Yangtze block, south China: SIMS U-Pb dating, *in-situ* Hf-O isotopes, and tectonic implications. *J. Asian Earth Sci.* 151, 101–111. doi:10.1016/j.jseaes.2017.10.029

Zhou, X. M. (2003). My thinking about granite genesis of south China. *Geol. J. China Univ.* 9 (4), 556–565. (in Chinese with English abstract). doi:10.3321/j.issn:1000-2383.2005.06.005

Zhou, X. M., Sun, T., Shen, W. Z., Shu, L. S., and Niu, Y. L. (2006). Petrogenesis of Mesozoic granitoids and volcanic rocks in South China, a response to tectonic evolution. *Episodes* 29, 26–33. doi:10.18814/epiiugs/2006/v29i1/004

Zindler, A., and Hart, S. (1986). Chemical geodynamics. *Annu. Rev. Earth Planet. Sci.* 14, 493–571. doi:10.1146/annurev.ea.14.050186.002425